

Hubble Space Telescope Captures UGC 12591: Bulge/Disk Properties, Star Formation and ‘Missing Baryons’ Census in a Very Massive and Fast Spinning Hybrid Galaxy

Shankar Ray,^{1*} Joydeep Bagchi,^{2†} Suraj Dhiwar,^{1,3,4} Mahadev B. Pandge,^{1‡} Mohammad Mirakhor,⁵ Stephen A. Walker,⁵ Dipanjan Mukherjee,³ Joe Jacob,⁷ Biju K. George⁸

¹Dayanand Science College, Latur 413531, India

²Department of Physics & Electronics, CHRIST (Deemed to be University), Hosur Road, Bengaluru 560029, India

³Inter-University Centre for Astronomy and Astrophysics, Pune 411007, India

⁴Savitribai Phule Pune University, Pune 411007, India

⁵The University of Alabama in Huntsville, OPB430 Huntsville AL, 35899, U.S.A.

⁶Department of Physics, Newman College, Thodupuzha 685585, India

⁷Department of Physics, W.M.O. Arts and Science College, Muttil P.O., North Kalpetta, Wayanad, Kerala, India

Accepted XXX. Received YYY; in original form ZZZ

ABSTRACT

We present Hubble Space Telescope (HST) observations of the nearby ($z = 0.023$), very massive, highly rotating (488.4 ± 12.5 km s⁻¹) hybrid (S0-Sa) galaxy UGC 12591, along with observations taken at other wavelengths from UV to FIR. Deep HST data of the galaxy in V, I and H bands is used to disentangle its bulge and disk components. The surface brightness distributions show a dominance of the bulge component over the disk with H-band bulge-to-disc luminosity ratio $\sim 69\%$. From spectral energy distribution (SED) fitting, we find an extremely low global star formation rate (SFR) of $\sim 0.1 - 0.2 M_{\odot} \text{y}^{-1}$, which is unusually low for this galaxy’s huge stellar mass ($M_{\star} \sim 1.6 \times 10^{11} M_{\odot}$), that implies a strong quenching of its SFR. For at least past 10^8 years the galaxy has remained in the quiescent state as a sterile, ‘red and dead’ galaxy. The fraction of total infra-red dust luminosity contributed by the ISM dust is as high as $\sim 90\%$, with total dust luminosity $L_{\text{dust}} = (0.5 - 3.5) \times 10^{10} L_{\odot}$, dominated by cold dust at equilibrium temperature $T_{\text{C}} \approx 15\text{K}$. UGC 12591 is found host to a super massive black hole (SMBH) of mass $6.18 \times 10^8 M_{\odot}$ which at the present moment is quiescent, i.e., neither we see large ($> 1\text{kpc}$) radio jets nor is the black hole contributing significantly to the mid-IR SED, ruling out the presence of strong radiative feedback from a bright AGN. We have obtained a detailed census of all observable baryons in this galaxy. The star formation efficiency is very low ($\sim 0.02 - 0.06$) and within a virial radius the galaxy has a total observed baryonic mass of $6.87 \times 10^{11} M_{\odot}$, amounting to a baryonic deficiency of $\sim 80\%$ relative to the cosmological mean. A small fraction of these cosmic baryons reside in a warm/hot circum-galactic halo phase, while the majority of baryons are still not observable. We have discussed various astrophysical scenarios for explaining its unusual physical properties. Our work is a major step forward in understanding the assembly history of such extremely massive, isolated galaxies.

Key words: galaxies: ISM – Galaxy: formation – galaxies: spiral – Galaxy: fundamental parameters – galaxies: individual: UGC12591

1 INTRODUCTION

Explaining galaxy formation in the Universe across cosmic time, within the current, widely accepted Cosmological paradigm known as the concordance Λ CDM cosmology, is one of the most important goals of astronomy research. It is believed that a number of physical processes are responsible for the observed galaxy properties, and identifying the correct ones among them is one of the principal goals of current galaxy formation theory. Star formation rate (SFR)

reached its peak at ‘cosmic high noon’ near $z = 2$ when galaxies rapidly built up their stellar masses by converting cosmic baryons to stars, and subsequently, over next billions of years the SFR went down drastically, and by the present era most of the massive galaxies have stopped growing, entering in a quiescent state (Behroozi et al. 2010, 2019; Moster et al. 2013). For reasons still unclear, even now some lower mass galaxies are still actively forming stars and massive local galaxies with halo mass $\gtrsim 10^{12} M_{\odot}$ have low specific star formation rate compared to less massive spirals (see Wechsler & Tinker (2018) for a review).

The formation era of progenitors of these massive galaxies is debatable, but it could stretch as far back in time as $z > 6$, when they gradually grew in mass as well as formed new stars from cosmic

* E-mail: rays71349@gmail.com

† E-mail: joydeep.bagchi@christuniversity.in

‡ E-mail: mbpandge@gmail.com

baryons. Near redshift $z = 2$, when the Universe was about three billion years old, half of the most massive galaxies were in place as compact proto-galaxies and they had already exhausted their fuel for star formation. Of the rest, about 25% galaxies assembled before the peak of the cosmic star-formation, while 25% galaxies formed later (Madau & Dickinson 2014). At higher redshifts, it is observed that most of them were harboring intense nuclear starbursts and possibly they ultimately grew into the most massive local galaxies seen today, through mergers with minor companions and gas accretion from cosmic-web filaments. Unveiling how this remarkable transformation happened and what physical factors were behind this change has been an enduring quest, which brings forth some of most hotly debated, key questions in galaxy formation (for reviews see Vogelsberger et al. (2020) and Somerville & Davé (2015)).

One of the prime drivers of suppression and even halting of star formation in galaxies is believed to have operated via a process called the AGN (Active Galactic Nuclei) feedback. When supermassive black holes (SMBH) growing at the centres of galaxies accrete matter, they turn into powerful engines (Lynden-Bell 1969) that can potentially heat and even expel the gas of their host galaxies, thereby halting star formation (Somerville et al. 2008; Di Matteo et al. 2005; Beckmann et al. 2017). It is now widely recognized that in our local Universe such SMBHs of masses $\sim 10^6 - 10^{10} M_{\odot}$ lurk in the nuclei of almost all massive galaxies (see Kormendy & Ho (2013) for a review). AGN feedback is likely to be more effective in massive galaxies because a remarkable tight coupling exists between the mass of the black hole and the galaxy's bulge and the total stellar mass/luminosity, which suggests that; (a) mass of the central SMBH will be higher in massive bulge dominated galaxies and so will be its energetic output and impact on the surroundings (b) the star formation rate and final mass of the galaxy has somehow been regulated symbiotically by the black hole over cosmic time, e.g., (Magorrian et al. 1998; Gebhardt et al. 2000; Häring & Rix 2004; Marconi & Hunt 2003; Gültekin et al. 2009; Sahu et al. 2019). In spite of the popularity of AGN feedback models, there is no good understanding of exactly how the AGN is fuelled and how the radio jets or hot outflows from the SMBHs deposit energy to their surroundings, the energy that is transferred to the different gas phases, and what are the physical conditions when significant positive or negative feedback on star formation rate is produced (see review by Fabian (2012)). Despite numerous efforts to observe SMBHs in the process of quenching star formation, conclusive evidence for such a process has remained elusive, particularly in the nearby Universe. The impact of AGN feedback via radio jet mode on the hot intracluster medium (ICM) is observed directly through X-ray observations of the cavities and bubbles around the central galaxies of cool core clusters.

Some observations have recently confirmed AGN feedback scenario locally for galaxies, e.g. (Martín-Navarro et al. 2018). Recent Carbon Monoxide and radio observations of a super massive, jetted spiral galaxy 2MASX J23453268-0449256 (J2345-0449 hereafter) (Bagchi et al. 2014; Nesvadba et al. 2021) and relativistic hydrodynamic simulations of radio jets propagating in a dense ISM (Mukherjee et al. 2016; Mandal et al. 2021) provide strong support for AGN-jet feedback scenario. Interstellar turbulence may play a major role in quenching star formation in AGN hosted galaxies, as shown by observations and recent hydrodynamic simulations (Nesvadba et al. 2010; Lanz et al. 2016; Federrath & Klessen 2012; Mandal et al. 2021; Mukherjee et al. 2016).

The Circum Galactic Medium (CGM), around galaxies plays a most important role in deciding, at all cosmological epochs, how galaxies acquire, eject, and recycle their gas, which in turn are the most important physical factors in determining how the galaxies

evolve, how much star formation will take place, or even how much of it will be quenched or is recycled back. Apart from the unseen dark-matter, the CGM is an extremely dynamic environment having a complex mix of baryons existing in various phases of temperature, density and metal content, which presents an extremely important but perhaps the least understood aspect of galaxy formation (see Tumlinson et al. 2017) for a review). Among the many interesting and challenging problems that the CGM presents, one of the most perplexing issues has been the so called 'missing baryons' problem. The term 'missing baryons' refers to the fact that even in multi-wavelength observations of galaxies, the total detectable baryonic mass falls far short (by 50 to 80 %) of the cosmic baryon fraction of $\approx 0.15 - 0.17$ as expected in Λ CDM cosmology, based on Big Bang nucleosynthesis and Cosmic Microwave Background constraints. A number of theories and simulations have tried to explain why only a small fraction of these halo baryons condenses into stars and why by $z = 0$ the star formation efficiency f_{\star} reaches a peak of about 20 - 30% for typical L_{\star} galaxies. For very massive galaxies (halo mass $\gtrsim M_h \sim 10^{12} M_{\odot}$), beyond the peak, f_{\star} declines rapidly to $f_{\star} \sim 2 - 5\%$ at $M_h \sim 10^{13} M_{\odot}$ (Schaye et al. 2015; Behroozi et al. 2010, 2019; Moster et al. 2013). It is believed that AGN feedback is one of the main factors needed to bring this decline in SFR of most massive galaxies. A similar decline in SFR is seen on the lower mass end of the peak ($\lesssim M_h \sim 10^{12} M_{\odot}$), attributed to supernova feedback.

Leading galaxy formation theories (White & Rees 1978; White & Frenk 1991; Fukugita & Peebles 2006; Sommer-Larsen 2006) demand a warm-hot X-ray corona containing a large fraction (at least 50%) of cosmic baryons in such massive galaxies. Observing such baryon filled halos have been elusive so far. To validate galaxy formation models and make a census of baryons we need sensitive X-ray or UV observations of galactic halos. It has been proved very challenging to detect the hot gaseous corona around even very luminous spirals and ellipticals with our present telescopes due to sensitivity limitations. With XMM-Newton such coronas have been robustly detected in only a handful of galaxies so far, e.g., (Dai et al. 2012; Mirakhor et al. 2021; Walker et al. 2015; Anderson & Bregman 2011; Anderson et al. 2016; Bregman et al. 2018; Bogdán et al. 2013) and independent constraints on their temperature, density, and metallicity from soft X-ray spectroscopy is still lacking. These galaxies provide compelling evidence for the existence of hot, low-metallicity atmospheres of gas that could originate with accretion from the IGM and subsequent heating to the virial temperature of the halo via accretion shocks. However, the fraction of baryons residing in the hot phase, and its dependence on stellar and or halo mass, as well as how they are affected by galactic feedback and star formation processes are not well determined and poorly understood so far.

Our target UGC 12591 (232521.75+282942.76 J2000.0) at a redshift of $z=0.023$ is classified as a S0/Sa type isolated galaxy located at the western-most fringes of Perseus-Pisces supercluster. It is a giant, hybrid-morphology galaxy showing both an extended ellipsoidal stellar bulge, girdled by an equatorial disc of gas and dust. By any standards it has exceptional physical properties which sets it apart from most galaxies. It has some resemblance to the nearby Sombrero galaxy (NGC 4594), although UGC 12591 is much larger in size. Keplerian disc rotation velocity of UGC 12591 is extremely high, more than twice that of the rotational velocity of Milky way and one of the highest known so far. Following on the earlier results of Roberts (1978), Giovanelli et al. (1986) presented the 21 cm HI gas profile of UGC 12591 smoothed to an effective resolution of 25 km s^{-1} and

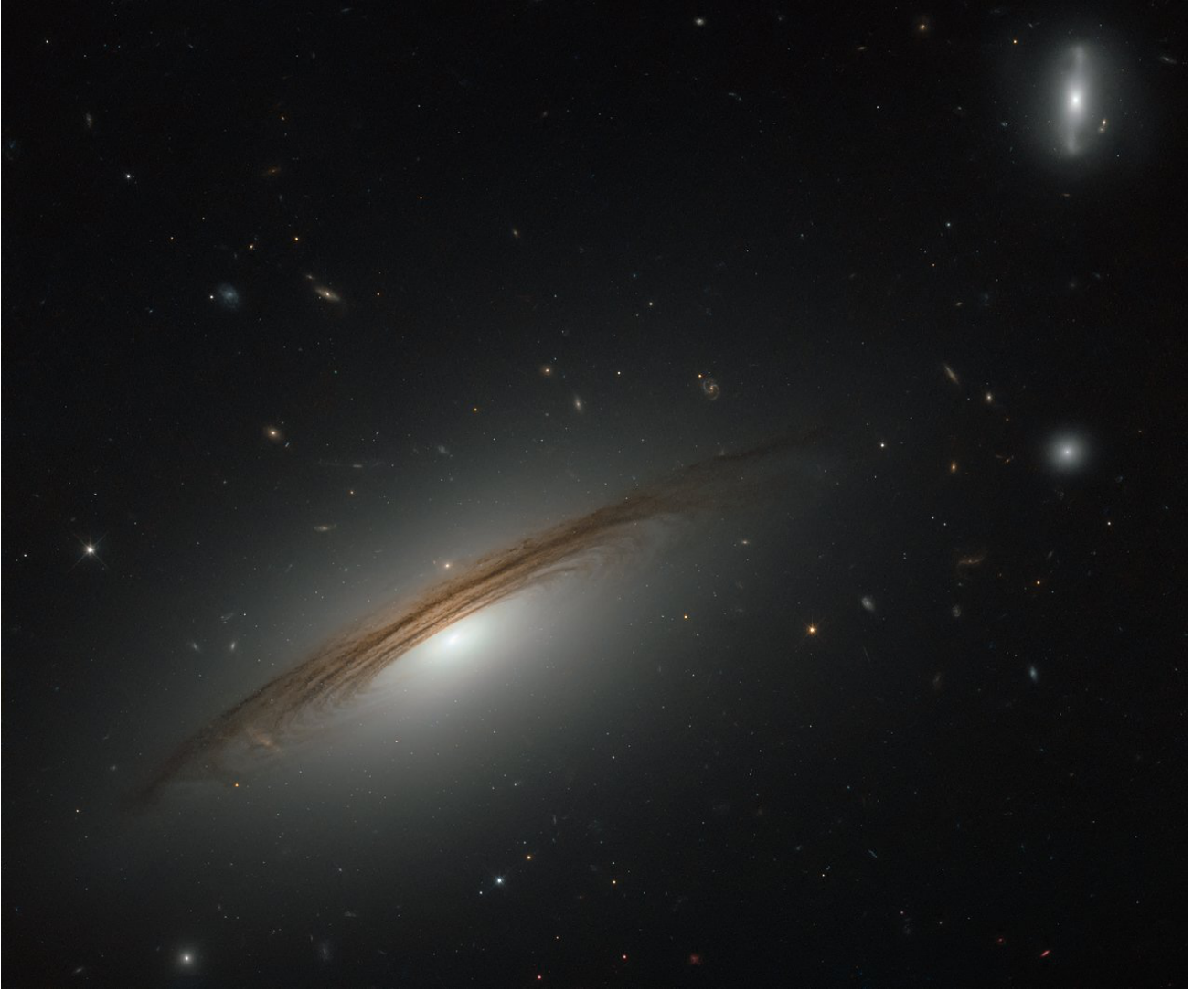


Figure 1. A colour image of the UGC 12591 is shown as imaged by *Hubble Space Telescope*. A massive stellar bulge and prominent, stratified dark dust lanes can clearly be seen crossing the equatorial plane and a bright, compact central nucleus is also noticeable. The barred spindle shaped satellite galaxy at upper right corner is WISEA J232529.77+283021.3 at redshift 0.0233, same as UGC 12591. Image credit: (ESA/Hubble and NASA)

reported the 50% peak line width of $W_{50} = 1014 \pm 10 \text{ km s}^{-1}$ and maximum rotational velocity (corrected for inclination and relativistic Doppler effect) of $v_{\text{rot}} = 506 \pm 6 \text{ km s}^{-1}$. They also measured similar high rotation velocity extending upto $\sim 20 \text{ kpc}$ from center, via $H\alpha$ and [NII] lines of ionized gas. This corresponds to the interior dynamical masses of $M_{\text{dyn}} = 1.16 \times 10^{12} M_{\odot}$ and $2.9 \times 10^{12} M_{\odot}$ at 20 and 50 kpc respectively, which are extremely large and comparable to the most massive spiral galaxies. With XMM-Newton Dai et al. (2012) detected a large, soft X-ray halo/corona emission out to $\sim 50 - 80 \text{ kpc}$ from the galaxy centre having X-ray luminosity $L_x(0.1 - 10 \text{ keV}) = 3.9 \times 10^{40} \text{ erg s}^{-1}$ and temperature of the halo gas of $T_{\text{halo}} = 0.64 \pm 0.03 \text{ keV}$, which showed that some fraction of baryon mass resides in an extended, circum-galactic warm-hot gaseous halo. This is an extremely important finding which has strong bearing on understanding the star formation history and baryon content of this and other massive galaxies.

Fig. 1 shows the optical color image made from HST WFC3 filters, where the existence of prominent, stratified dust lanes and the large extent of the galaxy's massive stellar bulge can be seen clearly. It is

possible that these stratified dust lanes are spiral arms seen in projection. Another small satellite galaxy WISEA J232529.77+283021.3 can be seen in the picture.

For UGC 12591 excellent quality data of *Hubble Space Telescope* (hereafter HST) has been taken and here we present a detailed photometric study of this galaxy using three colour data in F160W, F606W & F814W bands, respectively. In each band, we have decomposed the galaxy into its bulge and disk components and estimated the structural parameters associated to them.

We also present the best fitting spectral energy distribution (SED) of UGC 12591. The SED fitting has been done using two different software packages; (Sec. 2.5 and Sec. 2.4) for cross checking and for obtaining a number of ISM and stellar parameters. From these fittings we estimate various key properties of the galaxy, such as its star formation rate, stellar mass, dust mass, dust temperature and luminosity, gas mass, AGN fraction and baryon fraction etc. (Table 4, Table 5). In this paper we demonstrate how this giant galaxy possesses an extremely low star formation rate and a large repository of baryons

Table 1. Basic details of the HST data of UGC 12591.

Filter	Band	Configuration	ExpTime seconds	λ_{central} nm	pixel size arcsec/pixel
F606W	V	WFC3/UVIS	2619.00	588.8	0.039
F814W	I	WFC3/UVIS	2739.00	803.4	0.039
F160W	H	WFC3/IR	5596.93	1536.9	0.090

is still accounted for in any observation so far, and we discuss the astrophysical implications of our findings.

The structure of this paper is as follows. In §2. we describe the data. The data reduction strategy briefly for optical and near-IR observations is described in §3. and §4. Discussion, conclusions and summary of the study is outlined in §5. We assume $H_0 = 72 \text{ km s}^{-1} \text{ Mpc}^{-1}$, $\Omega_M = 0.26$ and $\Omega_\Lambda = 0.74$, translating to a scale of $0.452 \text{ kpc arcsec}^{-1}$ at the red-shift $z = 0.023$ of UGC 12591.

2 DATA ANALYSIS

2.1 HST observations and data

We have used the exquisite, HST multi-band archival data (HST Observing Program 13370, PI: Georgiev I.Y.) for UGC 12591 which was observed using the Wide Field Camera 3 (WFC3) in June 2014. WFC3 offers high resolution, sensitivity and wide field imaging capability over a wavelength range of near ultraviolet 200 nm to near infrared 1700 nm. WFC3 has two imaging channels, namely Ultraviolet-Visible (UVIS) and Infrared (IR). UVIS has a field of view of $162'' \times 162''$ for the wavelength range of 200 – 1000 nm with pixel scale of $0.039'' \times 0.039''$. The IR channel has a field of view of $136'' \times 123''$ for the wavelength range of 800 – 1700 nm with a pixel scale of $0.13'' \times 0.12''$. WFC3 provides a choice of 62 and 15 wide, medium and narrow band filters for UVIS and IR channel respectively with 1 grism in the UVIS and 2 in the IR channel. The UVIS detector operates in ACCUM mode in order to produce time integrated images. While IR detector operates in MULTIACCUM mode, where accumulated signal can be read out non-destructively multiple times without causing harm to other pixels.

Deep Observations were taken using age-metallicity sensitive, wide-band V, I, and H filter sets [V (F606W), I (F814W) and H (F160W)] respectively. F606W and F814W have rectangular band-passes of width 218.2 nm and 153.6 nm respectively, whereas F160W has bandpass of 268.3 nm. The peak system throughput of F160W, F606W and F814W are 0.56, 0.29 and 0.23 respectively. The background contamination has been significantly reduced by the high spatial resolution of WFC3 channels which is not achievable with ground based observations. The filter specific details about the HST data are tabulated in Table 1.

We retrieved all of the FITS images from Hubble Legacy Archive¹.

2.2 SED input data

Astronomical objects emit radiation in a broad possible range of colours. In spectral energy distribution (SED) fitting the radiative flux of any galaxy observed over the wide wavelength range is analysed to

¹ Based on observations made with the NASA/ESA Hubble Space Telescope, and obtained from the Hubble Legacy Archive, which is a collaboration between the Space Telescope Science Institute (STScI/NASA), the Space Telescope European Coordinating Facility (ST-ECF/ESA) and the Canadian Astronomy Data Centre (CADM/NRC/CSA)

Table 2. Radiative flux in different passbands (effective wavelength λ_{eff}) is shown which is used for the SED fitting by CIGALE and GALFIT. The data is taken from ¹NED & ²CDS.

Passband	λ_{eff} μm	Flux mJy	Flux Error mJy	References
GALEX FUV	0.1529	0.0307	0.00721	1
GALEX NUV	0.2312	0.0795	0.00638	1
SDSS u	0.3519	1.90	0.01	2
SDSS g'	0.4820	6.02	0.2893	2
SDSS r'	0.6247	16.3	0.8	2
SDSS i'	0.7635	27.2	1.7989	2
2MASS J	1.2390	62.9	0.232	1
2MASS H	1.6500	82.3	0.304	1
2MASS Ks	2.1640	73.9	0.273	1
WISE W1	3.3500	41.9	0.232	1
WISE W2	4.6000	22.8	0.126	1
WISE W3	11.560	17.3	0.230	1
WISE W4	22.090	11.3	1.40	1
IRAS 60	60.000	230	34	1
IRAS 100	100.00	1550	159	1

find out several physical parameters like the star formation rate (SFR), stellar mass, gas mass, dust properties and feedback contribution via AGN and stellar modes etc. In order to fit the SED, we have made use of the available data of wide wavelength range, spanning from GALEX in UV, SDSS in optical, 2MASS in near-IR, WISE in mid-IR and IRAS in the far-IR. The flux values from different telescopes as a function of central effective wavelength have been tabulated in Table 2.

2.3 Bulge-disk decomposition

Extremely high spatial resolution offered by HST has some definite advantages over ground-based imaging. For example, galaxies with central bulge and strong light concentration, a surface brightness profile in poor seeing conditions could give the illusion of a central light deficit. Atmospheric blurring also affects the fitted light profile creating spurious break/flattening on its slope. The above effect is more pronounced when the true light concentration is on a scale comparable or below the seeing which can mislead one to believe on the detection of a depleted core, which results due a dynamical influence of a super massive black hole (SMBH). HST can largely mitigate this problem. Moreover, the simultaneous fit of wide-wavelength range, high resolution HST images makes the bulge-disk decomposition more robust against such spurious effects.

The structural decomposition was done using GALFIT software (Peng et al. 2002) on the HST F606W, F814W and F160W band images. We first mask the foreground stars in the images. UGC 12591 contains thick dust lanes, primarily dominant in the UVIS bands (Fig. 2). Masking these dust lanes is necessary to avoid its effects on structural parameters obtained from the 2D fit. The masking was done using the IMEDIT task in IRAF (Tody 1986, 1993). After masking for unwanted sources and dust lanes for each of the filters the 2D decomposition is performed. We use the Point Spread Function (PSF) obtained from STScI for convolution while fitting, and used 1401×1401 pixel fitting region for F160W and 4001×4001 pixel region for both of F606W and F814W images centered on the brightest pixel of the object. To fit the image we specify the profile function as well as the initial estimates for the model parameters. For Sersic model these parameters are; position of the centre of the profile, integrated magnitude (mag), effective radius (r_e), Sersic index (n), axis ratio (b/a) and the position angle (PA). The best-fit model

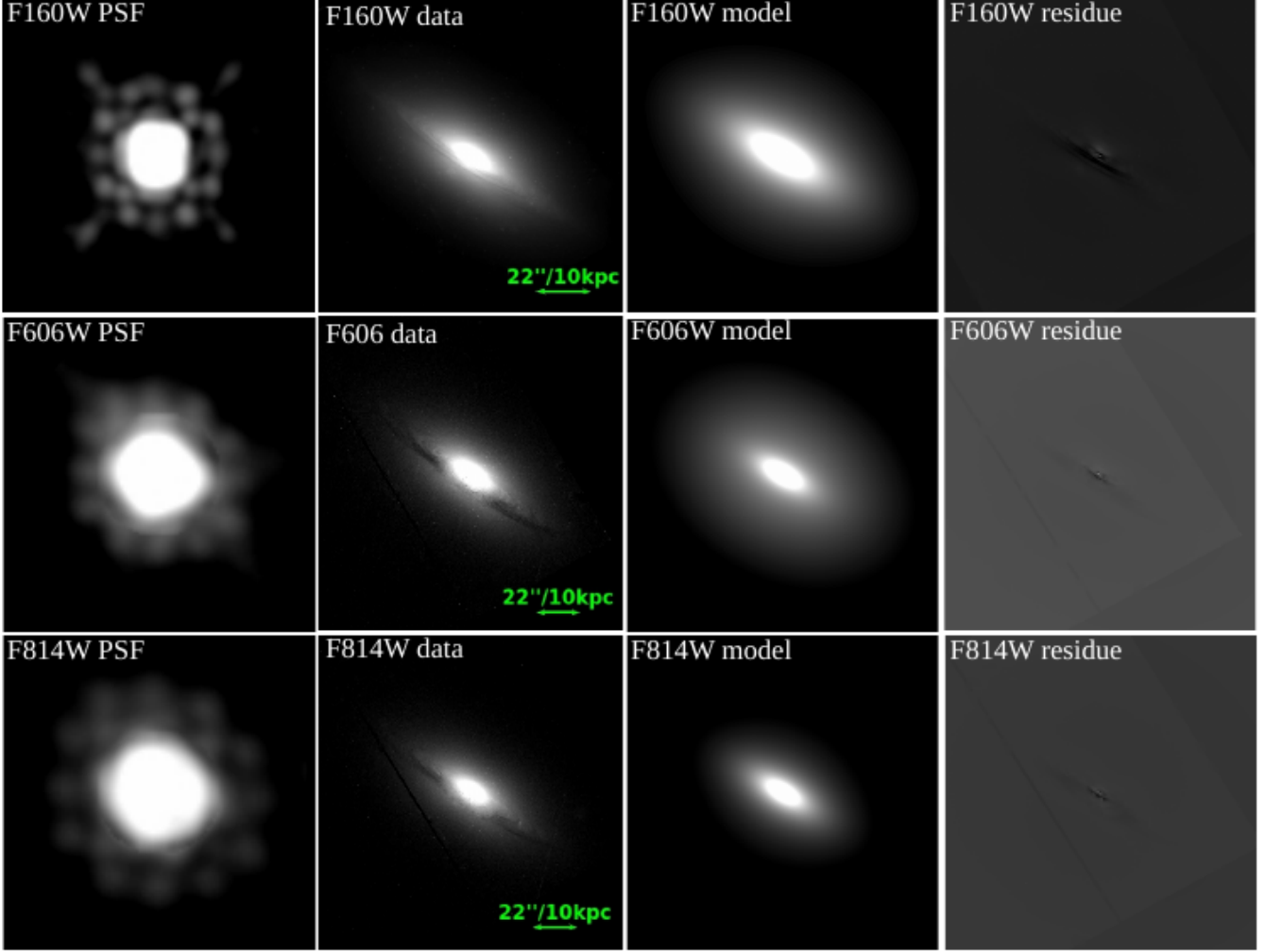


Figure 2. Images of the inner $126'' \times 126''$, $156'' \times 156''$ and $156'' \times 156''$ of galaxy UGC 12591 in three HST WFC3 filters: F160W (H band), F606W (V band) and F814W (I band) respectively, given as inputs to GALFIT are shown with a log scale (second column). The point spread functions (PSF) used in three filters are shown (left most column). The best fit models and their residues for each bands are shown (images in third and fourth columns). While fitting, to reduce the background contamination from other sources (mainly stars and galaxies) and for robust fits, the background has been masked for IR F160W image and the prominent dust lanes have been masked carefully for UVIS F606 and F814W images.

Table 3. Here the best fit parameters of GALFIT is shown in three filters H, I and V. The values in square brackets are held fixed (priors) during the modeling in order to achieve better results. The Sersic, Exponential and PSF function have seven, six and three free parameters respectively. In the table we exclude the central coordinates (x_0, y_0) of these functions in 2D fit that are also free parameters as these will vary for different pixel dimensions of images taken to fit. The magnitudes given here are in AB scale.

Filter	Band	Sersic Mag.	r_e	n	Sersic $\frac{p}{a}$	Sersic PA	Exp. Mag.	r_s	Exp. $\frac{p}{a}$	Exp. PA	PSF Mag.	N_{dof}	χ^2_V
-	-	mag	arcsec	-	-	deg	mag	arcsec	-	deg	mag	-	-
F160W	H	10.80	12.32	3.68	0.42	59.90	10.42	41.56	0.84	[59.00]	16.76	1962788	1.25
F814W	I	12.70	10.50	3.01	0.46	58.74	11.12	58.43	0.83	54.12	19.65	16007987	0.99
F606W	V	13.45	7.35	2.32	0.46	59.31	11.26	53.71	0.74	[59.00]	21.20	16007988	0.81

is produced through multiple iteration based on these initial parameters and then convoluted with the corresponding WFC3 PSF. The best-fit is based on χ^2_V minimization using the Levenberg-Marquardt downhill-gradient method. We have used the sigma image generated internally by GALFIT in this fit. Although we used the pipeline, we vary the initial conditions of different parameters to check whether the final results correspond to a global minimum. We found that the results are stable against different initial conditions.

Considering the disc morphology and a prominent bulge in UGC 12591, initially we model the surface brightness profile with two components, viz. Sersic model for the bulge and an exponential disc function. The Sersic profile is defined as,

$$\Sigma(r) = \Sigma_e \exp \left[-\kappa \left(\left(\frac{r}{r_e} \right)^{1/n} - 1 \right) \right] \quad (1)$$

Here, $\Sigma(r)$ and Σ_e are pixel surface brightness at radius r and r_e

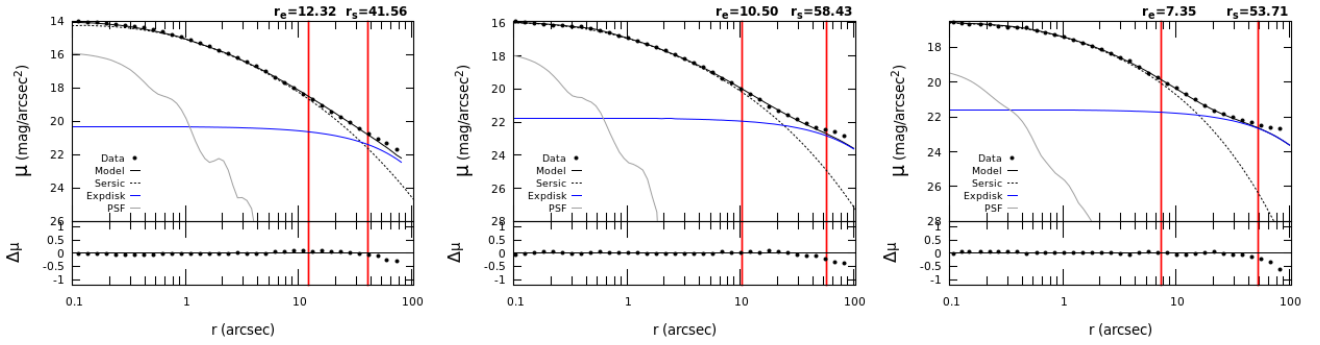


Figure 3. The left, middle and the right panels show the model and observed surface brightness profiles (μ in $\text{mag}/\text{arcsec}^2$) in F160W, F814W and F606W bands respectively. The composite model (black line) fitted through observed data (black dots) is decomposed into a Sersic profile, exponential disc profile and a PSF model which are shown in the legend. In bottom panels the residuals ($\Delta\mu$) between the model and data have been shown. In each plot the effective radius r_e corresponding to Sersic profile and the disk scale length r_s corresponding to the Exponential-disk profile (see Subsec. 2.3) are shown by vertical red lines. The best fit values of r_e , r_s and other parameters are listed in Table 3. For $r \leq r_e$ the resultant model in each band is highly dominated by the Sersic function. And for $r \geq r_s$ the model is dominated by Exponential-disk function. It is clearly seen from the plots for F606W (V) and F814W (I) that they have extended disk scale lengths. The near infra-red F160W (H) profile is highly bulge dominated and its disk scale length is also less than that for F606W and F814W. For the region where $r_e \leq r \leq r_s$, both the Sersic and the exponential functions contribute to the model significantly.

respectively, r_e is effective (half-light) radius, n is the Sersic index, and κ is a dependent variable coupled to n such that r_e encloses half of total brightness.

The exponential-disc function is defined as,

$$\Sigma(r) = \Sigma_0 \exp\left(-\frac{r}{r_s}\right) \quad (2)$$

Here, $\Sigma_0 = \Sigma(r)|_{r=0}$ and r_s is disc the scale length. The two component model fits well the bulge and the disc, however there remained on residual images an unresolved light excess at the centre of the galaxy, probably attributed to an AGN activity and/or a compact nuclear star cluster. To accommodate this excess light we added an additional PSF function along with the Sersic and exponential disk components. The results show a significant improvement of the residuals and model parameters. The final best fit results are given in Table 3 showing excellent reduced χ^2_ν and depicted in Fig. 2.

2.4 Surface brightness profiles of UGC 12591

The visualization of how good the modeling has been can be depicted in 1D radial profile plots even though the non-axisymmetric features of the surface brightness profiles are lost in this representation. After getting the models generated by GALFIT (Fig. 2), the `ellipse` routine of PYRAF/STSDAS was used to plot the surface brightness (μ) variation as a function of the semi-major axis distance (r) of the galaxy by fitting concentric elliptical isophotes of constant surface brightness. The procedure is applied to the final PSF convolved model as well as to the models corresponding to the sub components, such as the Sersic, exponential-disk and PSF, in each of the three bands to calculate individual contribution of the sub components to the composite light profile of the galaxy. The results are shown in the Fig. 3. The goodness of the fit is quantified by the residual $\Delta\mu$ shown, that indicates the difference between data and corresponding model. The contribution of the Sersic, exponential-disk and PSF profiles can be seen in each of the bands.

2.5 SED fitting with CIGALE

The SED fitting is done with the python based software CIGALE (Code Investigating Galaxy Evolution) (Boquien et al. 2019) which

extends the SED fitting algorithm written by Burgarella et al. (2005); Noll et al. (2009). We make use of all the available flux in literature over the wavelength (0.1 – 100 μm) range of far-ultraviolet to far-infrared (Table 2) and implement modules to compute the best fit SED which are: (1) *sfdelayed* for star formation history (Boquien et al. 2019) (2) *bc03* for stellar population (Bruzual & Charlot 2003) (3) *nebular* for nebular emission (Inoue 2011) (4) *dustatt_powerlaw* for dust attenuation (Boquien et al. 2019) (5) *dale2014* (Dale et al. 2014) for dust emission and (6) *redshifting* (Meiksin 2006). The SED fitting done by CIGALE is shown in Fig. 4. The model outputs consist of two peaks, one for stellar emission indicated by the blue dotted-line and one for the dust emissions indicated by red continuous line. The greenish-yellow lines designate the Nebular emission of ionized gas at different wavelengths.

We have also considered three SEDs modelled with different AGN fractions of 0%, 5% and $\sim 10\%$. It is defined as the AGN contribution to the total IR luminosity from $\sim 5\text{--}1000\mu\text{m}$. AGN fraction explicitly takes into account three emission components through a radiative transfer model: the primary source surrounded by a dusty torus, the scattered emission by dust, and the reprocessed thermal dust emission (Boquien et al. 2019). It can be seen from the SED fit parameters (Table 4) that as the AGN fraction is increased the χ^2_ν increases but the best fit parameters are not drastically changed. Thus we conclude that at present a powerful AGN (hosted by a supermassive black hole) is not contributing much to the mid-IR bands, ruling out the presence of strong radiative feedback from a bolometrically bright AGN. NVSS has detected a compact central radio source associated with UGC 12591 having luminosity of $L_{1.4\text{GHz}} = 3.01 \pm 0.92 \times 10^{32}$ W (Condon et al. 1998, 2002) which can possibly be attributed to radio emission of an AGN, although no large scale radio jets have been detected.

The results of SED fitting by CIGALE is shown in Table 4. Here we only mention the best fit parameters that are important for our analysis: (1) old stellar mass M_{\star}^{old} (M_{\odot}) (2) young stellar mass M_{\star}^{young} (M_{\odot}) (3) total stellar mass M_{\star} (M_{\odot}) (4) ISM gas mass of old stars $M_{\text{gas}}^{\text{old}}$ (M_{\odot}) (5) ISM gas mass of young stars $M_{\text{gas}}^{\text{young}}$ (M_{\odot}) (6) total ISM gas mass M_{gas} (M_{\odot}) (7) instantaneous star formation rate SFR ($M_{\odot}\text{yr}^{-1}$) and specific star formation rate $s\text{SFR} = \text{SFR}/M_{\star}$ (yr^{-1}) (8) SFR averaged over 10 and 100 Myrs (9) stellar Luminosity L_{\star} (Watt) (10) dust luminosity L_{dust} (Watt).

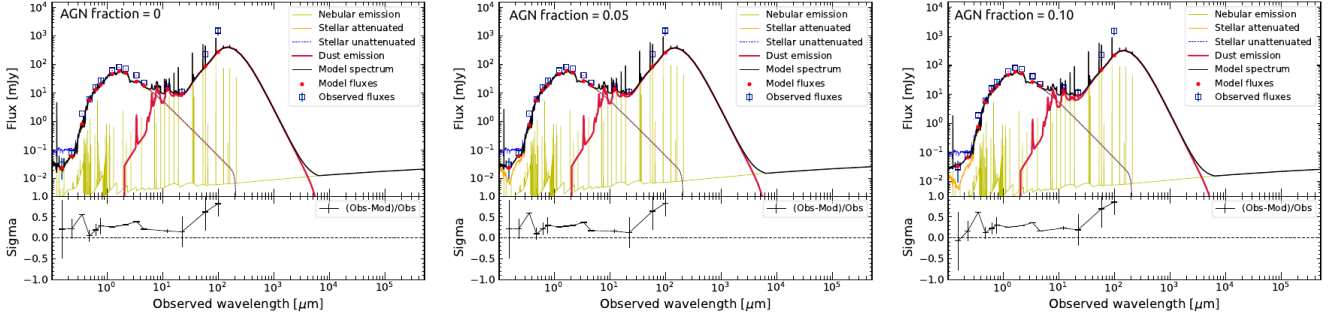


Figure 4. Here the Spectral energy distribution fitting of UGC 12591 using CIGALE has been presented for different AGN fractions. *Left:* AGN fraction = 0, *Middle:* AGN fraction = 0.05, *Right:* AGN fraction = 0.10. Observed flux over the wavelength range of 0.153 – 100 μm has been fitted to estimate some key parameters of galaxy shown in Table 4. Here sigma represents the relative residual flux. The blue squares are the input data points. The red dots are the best fit fluxes from SED fitting. Different ISM component contributing to SED fluxes are shown in the figure legends. No signature of strong radiative feedback from an AGN could be detected in the SED models.

Table 4. Here the best fit model parameters of the SED fitting by CIGALE is shown for different AGN fraction. The parameters mentioned from left to right are as follows: AGN – fraction that indicates contribution of an active galactic nuclei, M_{\star}^{old} – mass of older stellar population, M_{\star}^{young} – mass of younger stellar population, M_{\star} – total stellar mass, $M_{\text{gas}}^{\text{old}}$ – ISM gas mass of old stars gas, $M_{\text{gas}}^{\text{young}}$ – ISM gas mass of young stars, M_{gas} – total gas mass, SFR – instantaneous SFR, SFR₁₀ – SFR averaged over 10 Myrs, SFR₁₀₀ – SFR averaged over 100 Myrs, sSFR – specific star formation rate, L_{\star} – stellar luminosity, L_{dust} – dust luminosity, χ^2_{ν} – reduced chi square.

AGN fraction	M_{\star}^{old} $10^{11}M_{\odot}$	M_{\star}^{young} 10^5M_{\odot}	M_{\star} $10^{11}M_{\odot}$	$M_{\text{gas}}^{\text{old}}$ $10^{10}M_{\odot}$	$M_{\text{gas}}^{\text{young}}$ 10^4M_{\odot}	M_{gas} $10^{10}M_{\odot}$	SFR $M_{\odot}\text{yr}^{-1}$	SFR ₁₀ $M_{\odot}\text{yr}^{-1}$	SFR ₁₀₀ $M_{\odot}\text{yr}^{-1}$	sSFR 10^{-13}yr^{-1}	L_{\star} 10^{37}W	L_{dust} 10^{36}W	χ^2_{ν}
0.00	1.6	10.0	1.6	7.1	4.3	7.1	0.105	0.105	0.110	6.6	2.2	2.0	4.74
0.05	1.6	10.0	1.6	7.0	4.2	7.0	0.104	0.104	0.109	6.5	2.1	1.9	4.89
0.10	1.5	9.9	1.5	6.9	4.2	6.9	0.102	0.103	0.107	6.8	2.1	1.6	5.46

2.6 SED fitting with MAGPHYS

We also fitted the SED with the MAGPHYS package (Multi-wavelength Analysis of Galaxy Physical Properties (da Cunha et al. 2008)). This package allows to fit the whole SED, from the UV to the far-IR, by relating the optical and IR libraries in a physically consistent way. For the SED fitting we used 15 photometric bands, i.e. from the GALAX NUV to the IRAS 100 μm and computed the SED with the stellar-population synthesis models of (Bruzual & Charlot 2003). The wavelengths and flux values used for the SED fitting are listed in Table 2. The best fit SEDs were obtained by fixing the redshift to the $z=0.023$. The best fit output from the MAGPHYS package is shown in Table 5 and Fig. 5. In this figure the black solid line is the best-fit model to the observed SED and available data points are shown in red. The blue solid line shows the unabsorbed stellar spectrum. The bottom panel shows the residuals ($L_{\text{Obs},\lambda} - L_{\text{Model},\lambda} / L_{\text{Obs},\lambda}$). The lower part of the figure gives the likelihood distribution of several best fit physical parameters for UGC 12591. They are; (1) fraction of total dust luminosity contributed by dust in the ambient (diffuse) ISM (2) average V band dust attenuation, τ_V (3) Total effective V-band absorption optical depth of the dust seen by young stars inside birth clouds $\mu\tau_V$ (4) stellar Mass, $\log(M_{\star}/M_{\odot})$ (5) specific star formation rate, $\log(\text{sSFR})\text{yr}^{-1}$ (6) star formation rate, $\log(\text{SFR}/M_{\odot}\text{yr}^{-1})$ (7) total dust luminosity, $\log(L_{\text{dust}}/L_{\odot})$ (8) total dust mass, $\log(M_{\text{dust}}/M_{\odot})$ (9) equilibrium temperature of cold dust in the ambient ISM, $T_{\text{C}}^{\text{ISM}}/\text{K}$ (10) fractional contribution by cold dust to the dust luminosity of the ambient ISM, $T_{\text{W}}^{\text{BC}}/\text{K}$ (11) Total contribution by cold dust in the infrared emission, $\xi_{\text{C}}^{\text{tot}}$ and (12) Total contribution by warm dust in to the infrared emission, $\xi_{\text{W}}^{\text{tot}}$.

Table 5. SED fitting parameters of UGC12591 using MAGPHYS.

sSFR	M_{\star}	L_{dust}	M_{dust}	SFR	τ_V	$\mu\tau_V$	f_{μ}	T_{C}^{BC}	$T_{\text{C}}^{\text{ISM}}$	$\xi_{\text{C}}^{\text{tot}}$	$\xi_{\text{W}}^{\text{tot}}$
10^{-12}yr^{-1}	$10^{10}M_{\odot}$	$10^{10}L_{\odot}$	10^8M_{\odot}	$M_{\odot}\text{yr}^{-1}$				K	K		
3.0	9.5	3.5	4.1	0.286	2.4	0.62	0.905	36.9	15.4	0.836	0.096

3 DISCUSSION

3.1 Bulge-Disk structure of UGC 12591

The morphology of UGC 12591 has been decomposed into two principal components of Sersic bulge and exponential disk. The surface brightness profiles of the galaxy are presented in Fig. 3 where r_e and r_s are the scaling parameters of the bulge and disk components. It can be seen that the bulge effective radius r_e (§ 2.3) ranges from 3.3 – 5.6 kpc (Table 3) which indicates the extent of the bulge of the galaxy. From V to H band the value of r_e also increases, i.e. bulge is more prominent at longer wavelengths due to dominance of old stellar population in bulge.

On the other hand, disk scale length r_s (Eq. 2) is around 24.3 – 26.4 kpc in V and I which decreases to 18.8 kpc in H band. Bertin & Arnouts (1996) finds that the wavelength dependence of the scale lengths is due to the dust extinction. MacArthur et al. (2003) shows that the disk scale length decreases at longer wavelength due to higher concentration of older stars and dust in the central region relative to the outer disk region where the probability of star formation is higher (Möllenhoff 2004). The ratio of bulge effective radius to disk scale length (r_e/r_s) for V, I and H band are given by approximately 0.14, 0.18 and 0.30 respectively, showing increment of this ratio as band wavelength increases.

Sersic index n for UGC 12591 shows the same pattern as the effective radius r_e . Bulge n increases from 2.32 to 3.68 (Table 3) in V to H bands. This falls in the range of classical bulges which

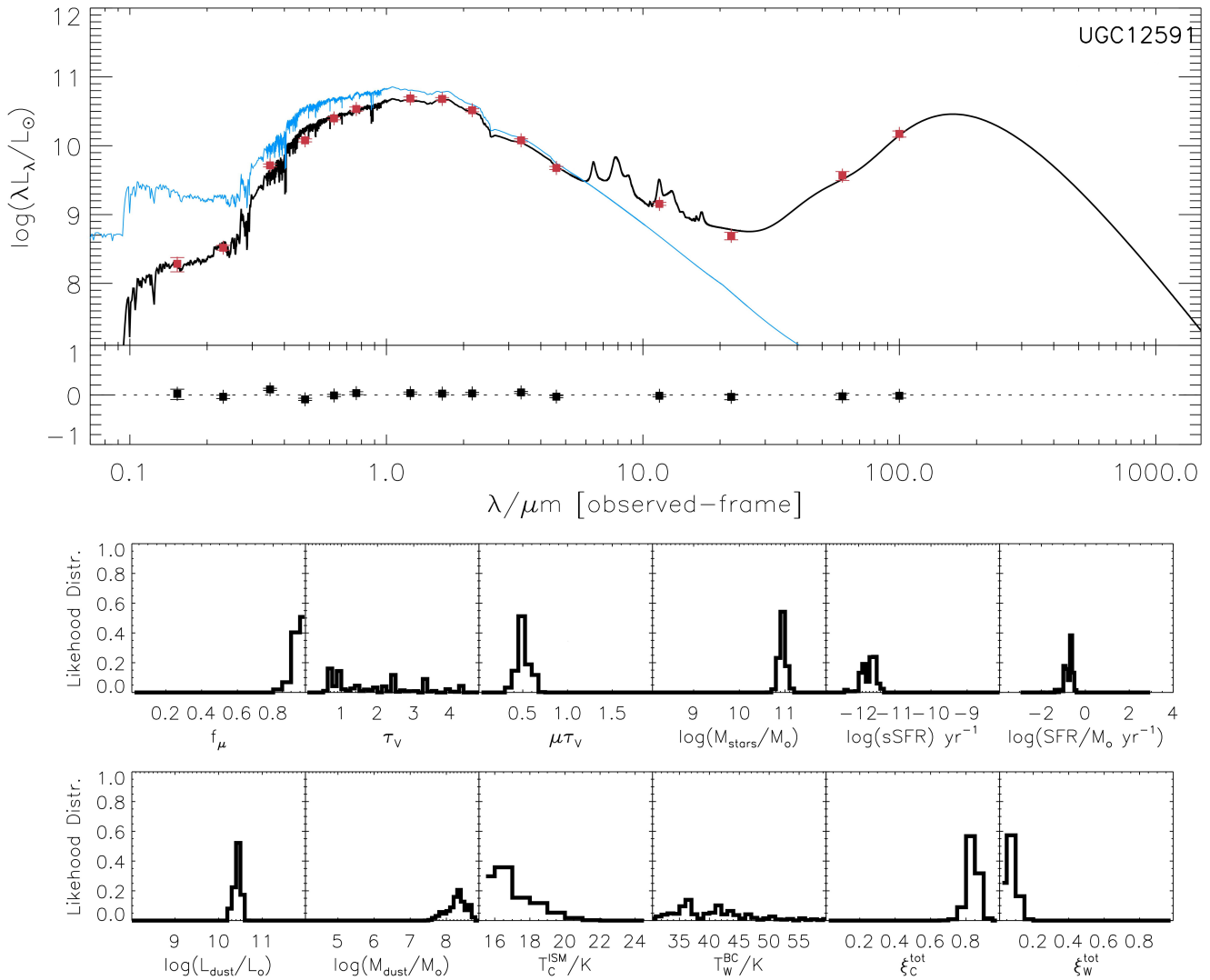


Figure 5. Result of SED fitting with *MAGPHYS* is shown here. The black solid line is the best-fit model to the observed SED with $\chi^2 = 3.96$, and observed flux data points are shown in red. The data points are composed of two GALEX, four SDSS, three 2MASS, two IRAS, and four WISE bands. The blue solid line shows the unabsorbed stellar spectrum. The bottom panel shows the normalised residuals. The lower part of the figure gives the likelihood distribution of best fit physical parameters for UGC 12591. These are; (1) fraction of total luminosity contributed by dust in the ambient (diffuse) ISM, f_μ (2) average V band dust attenuation, τ_V (3) Total effective V-band absorption optical depth of the dust seen by young stars inside birth clouds $\mu\tau_V$, (4) Stellar Mass, $\log(M_\star/M_\odot)$, (5) specific star formation rate, $\log(\text{sSFR}) = \log(\text{SFR}/M_\star) \text{ yr}^{-1}$, (6) star formation rate, $\log(\text{SFR}/M_\odot \text{ yr}^{-1})$, (7) total dust luminosity, $\log(L_{\text{dust}}/L_\odot)$, (8) total dust mass, $\log(M_{\text{dust}}/M_\odot)$, (9) equilibrium temperature of cold dust in the ambient ISM, $T_c^{\text{ISM}}/\text{K}$, (10) equilibrium temperature of warm dust inside the birth clouds, T_w^{BC}/K , (11) Total contribution by cold dust in the infrared emission, ξ_c^{tot} and, (12) Total contribution by warm dust in the infrared emission, ξ_w^{tot} .

have a much more centrally peaked light profile, contain a higher fraction of total light, and their Sersic index is larger ($n \approx 2-6$) than pseudo-bulges, which have $n < 2$ (Fisher & Drory 2008). The ratio of rotation velocity to central velocity dispersion $v_{\text{rot}}/\sigma_\star \sim 1.7$ is high for a bulge dominated system. Thus, along with bulge dispersion support, rotation support plays a major role in the dynamics of this galaxy.

Looking at the bulge (Sersic) magnitudes it can be seen that the bulge rapidly becomes brighter from V to H as n increases. This proves that UGC 12591 indeed is a bulge dominated disc galaxy as is obvious from Fig. 3. Möllenhoff (2004) showed that the bulges in early-type spirals are brighter, similar to the elliptical galaxies, and larger than that of the late-type galaxies for which the bulges

are comparable to their disks. The possible reason is that preeminent bulges of early-type spirals could have formed due to early mergers, which possibly explains structural properties of UGC 12591.

3.2 The bulge-to-disc mass and luminosity ratios

In Table 6 we show the bulge and disc parameters of UGC 12591 derived using *GALFIT* in three HST colours. Mass and luminosity of bulge and disc components are denoted by M or L with indicative subscripts. The B/D and B/T parameters represent the luminosity ratios of bulge to disc and bulge to total (bulge+disc) components respectively. Both these parameters are strongly colour dependent. The mass and luminosity of bulge component is largely dominated

Table 6. Here, we show the bulge and disk mass (M) and luminosity (L) parameters of UGC 12591 derived using GALFIT best fit magnitudes shown in Table 3. We have used Bell & de Jong (2001) to calculate the mass to light ratios, which are 0.68 (H-band), 1.34 (I-band) and 1.78 (V-band). The B/D and B/T represent the luminosity ratios of bulge to disc and bulge to total (bulge+disc) components respectively.

Band	L_{bulge} $10^{10}L_{\odot}$	L_{disk} $10^{11}L_{\odot}$	M_{bulge} $10^{10}M_{\odot}$	M_{disk} $10^{11}M_{\odot}$	$\frac{B}{D}$	$\frac{B}{T}$
H	31	4.5	21	3.1	0.69	0.41
I	5.1	2.2	6.8	2.9	0.23	0.19
V	3.1	2.3	5.5	4.1	0.13	0.12

by old stellar population contributing more to the H band NIR flux than in optical V band.

3.3 Interpreting dust mass and dust emission

UGC 12591 possesses a prominent disc of interstellar dust and cold, neutral HI gas in the equatorial plane. Based on our SED fitting (Table 5) we highlight the properties of the dust component here. Rowlands et al. (2012) did a study on dust properties and star formation history of the local sub millimetre detected galaxies, with some of them being early-type and passive spirals. The passive spirals are defined as early-type galaxies with dust abundance and low SFR. They found the mean $\log M_{\text{dust}} = 7.74M_{\odot}$ with M_{dust} in the range $10^5 - 10^8M_{\odot}$ for early-type galaxies, and for passive spirals mean $\log M_{\text{dust}} = 7.47$ with M_{dust} in the range $10^6 - 10^8M_{\odot}$. From SED fitting we find $\log M_{\text{dust}} = 8.6M_{\odot}$ (Table 5 and Fig. 5) consistent with the results of Rowlands et al. (2012), with dust mass for UGC 12591 falling in the highest end of passive spirals. The ratio $M_{\text{dust}}/M_{\star} \approx 0.002$ is typical of passive galaxies (Orellana et al. 2017).

The estimated equilibrium temperature of cold dust in the ambient ISM is $T_{\text{C}} \approx 15\text{K}$ and warm dust temperature $T_{\text{W}} \approx 37\text{K}$. In our SED fitting a single black body mean temperature is assumed for the cold dust. More likely, a continuous range of temperatures, heated by emission sources is needed (Bendo et al. 2015). We find f_{μ} , the fraction of total Infra-red dust luminosity contributed by the ISM dust is as high as 0.91 with total dust luminosity $L_{\text{dust}} = (0.5 - 3.5) \times 10^{10}L_{\odot}$ (Table 4 and Table 5), much higher than the mean $f_{\mu} = 0.58$ for normal L_{\star} spiral galaxies in Rowlands et al. (2012). However in L_{dust} , the cold dust contribution is much higher, $> 80\%$ compared to warm dust $< 10\%$ (Table 5 and Fig. 5). This is broadly consistent with the findings of Orellana et al. (2017) and da Cunha et al. (2010) that, on $L_{\text{dust}} - M_{\text{dust}}$ plane placement of a galaxy is most sensitive to the temperature of the cold component, rather than the values of L_{dust} or M_{dust} . This shows that UGC 12591 is a passive galaxy in which the ISM dust luminosity has domination of older stellar population responsible for modest dust heating rather than from hot, new born stars. This is further confirmed by calculations of star formation rate presented below. Future observations in millimeter/sub-mm and far IR bands ($\sim 100 - 1000 \mu\text{m}$) will better constrain the molecular gas and dust properties of this galaxy.

3.4 Star formation

3.4.1 SED derived star formation rate

We calculated the integrated star formation rate of UGC 12591 by SED fittings and obtained $\text{SFR}_{\text{SED}} \approx 0.115M_{\odot}\text{yr}^{-1}$ from CIGALE and $\text{SFR}_{\text{SED}} \approx 0.29M_{\odot}\text{yr}^{-1}$ from MAGPHYS (Table 5), which are

consistent within errors. Li et al. (2017) estimated the SFR of $1.17 \pm 0.13M_{\odot}\text{yr}^{-1}$ with WISE $22\mu\text{m}$ data. Apparently, our estimate is lower and probes recent star formation as it takes into account the UV, NIR and nebular fluxes. The star formation history (SFH) of UGC 12591 over the past $10^7 - 10^8$ yrs is extremely low and doesn't differ much from the present day instantaneous star formation rate (Table 4). Evidently, all major growth in stellar mass should have happened before this time period and for at least past 10^8 yrs the galaxy has remained in the quenched state as a sterile, 'red and dead' galaxy as is evident in Fig. 6.

3.4.2 FUV derived star formation rate

The FUV emission is a good tracer of young stellar population and SFR upto ~ 100 Myr. We estimate the SFR using the FUV magnitude (20.62 mag AB) from the GALEX catalog. The magnitude is corrected for dust extinction assuming $R_{\text{FUV}} = 8.01$ (Wall et al. 2019) and $E(B-V)=0.09$ in the direction of UGC 12591 obtained from IPAC dust maps. The corrected FUV magnitude of UGC 12591 thus estimates is (19.85 mag AB) corresponding to $F_{\lambda}=5.42 \times 10^{-16} \text{ ergs s}^{-1} \text{ cm}^{-2} \text{ \AA}^{-1}$ ($F_{\nu} = 4.22 \times 10^{-28} \text{ ergs s}^{-1} \text{ cm}^{-2} \text{ Hz}^{-1}$) and luminosity $L_{\text{FUV}}=4.66 \times 10^{26} \text{ ergs s}^{-1} \text{ Hz}^{-1}$. We then use the (Kennicutt 1998) relation to estimate FUV SFR;

$$\text{SFR}_{\text{FUV}} (M_{\odot}\text{yr}^{-1}) = 1.4 \times 10^{-28} L_{\text{FUV}} (\text{ergs s}^{-1} \text{ Hz}^{-1}) \quad (3)$$

The estimated SFR is $0.06 M_{\odot}\text{yr}^{-1}$ showing exceptionally low recent star formation activity, consistent with SED derived SFR above.

3.4.3 Why is the SFR so low ?

In Fig. 6 it can be seen that UGC 12591 when compared to the main sequence of star forming galaxies (Elbaz et al. 2007) falls at least 2 dex below this line due to its very low SFR. The optically luminous massive spirals and lenticular galaxies from Ogle et al. (2019a) with $M_{\star} \gtrsim 10^{11}M_{\odot}$ also fall below the main sequence line, but are placed much above UGC 12591. Some of the massive, isolated spiral galaxies from Li et al. (2017) with $M_{\star} \gtrsim 10^{11}M_{\odot}$ have also been shown. These isolated galaxies fall in the lower right region of the plot. It is interesting to note that UGC 12591 falls farther in the lower part of the diagram, in the region predominantly occupied by galaxies with nearly or fully quenched star formation activity of Kalinova et al. (2021).

On the right hand side of Fig. 6 it can be seen that when compared to sequence of UV bright star forming galaxies, UGC 12591 is located in the lower-most region of quiescent galaxies showing the lowest specific sSFR of all. In the same region is located J2345-0449, another very massive and highly rotating spiral galaxy studied by Bagchi et al. (2014); Nesvadba et al. (2021). Position of both galaxies is in stark contrast with the ultraviolet luminous galaxies of Hoopes et al. (2007) which show far more recent star forming activity for the same mass range. Low SFR of both these very massive galaxies ($M_{\star} > 10^{11}M_{\odot}$) located in sparse environment show that galaxy's mass and local environment is responsible to quench star formation. We plot two other massive spirals NGC 1961 and NGC 6753 which have low, partially quenched sSFR, in accordance with their large mass $\log(M_{\star}) > 11.5$. There are still very few studies of cold molecular gas content of galaxies falling below the main sequence of star formation, and a general perception is that these systems are devoid of gas. However a detailed study of their molecular gas content is a key element for understanding the reason behind their remarkably low SFR.

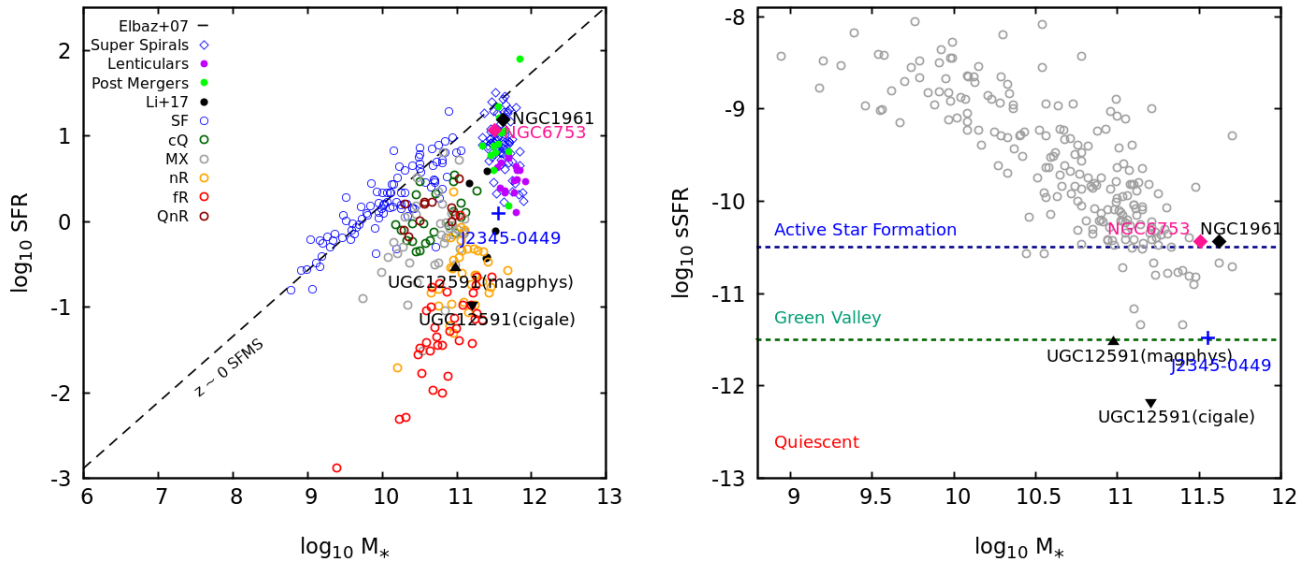


Figure 6. Left: Here, the variation of SFR ($M_{\odot}\text{yr}^{-1}$) with stellar mass M_{\star} (M_{\odot}) has been shown for galaxies of various types. The dotted line indicates the star forming main sequence from $z \sim 0$ (Elbaz et al. 2007). Super spirals, lenticulars and post-mergers are taken from Ogle et al. (2019a). Li et al. (2017) indicates the isolated massive spiral galaxies. Galaxies with different quenching stages like the star forming (SF), centrally quenched (cQ), mixed (MX), nearly retired (nR), fully retired (fR) and quiescent-nuclear-ring (QnR) taken from Kalinova et al. (2021) have also been shown. UGC 12591 with $M_{\star} = 1.6 \times 10^{11} M_{\odot}$ and $\text{SFR} = 0.105 M_{\odot}\text{yr}^{-1}$ from CIGALE, falls in the region of highly quenched fR galaxies. For comparison, another extremely massive and fast rotating spiral J2345-0449 from (Bagchi et al. 2014; Nesvadba et al. 2021) and other massive spirals like NGC 1961 (Anderson et al. 2016) and NGC 6753 (Bogdán et al. 2013) are also plotted in both the graphs. Right: Here the specific star formation rate (sSFR in yr^{-1}) versus the stellar mass (M_{\star} in M_{\odot}) is shown for star forming ultraviolet luminous galaxies taken from Hoopes et al. (2007). On both panels data point labeled CIGALE and MAGPHYS represent the estimates for UGC 12591 with sSFR and stellar mass from CIGALE and MAGPHYS respectively. Roughly $\log_{10} \text{sSFR} > -10.5$ is the region of galaxies with active star formation, $-11.5 < \log_{10} \text{sSFR} < -10.5$ corresponds to green valley and galaxies with $\log_{10} \text{sSFR} < -11.5$ represents the region of truly quiescent galaxies (Salim et al. 2016). It can be seen that galaxy UGC 12591 occupies a position in the lower right due to its highly quenched state where another massive and quenched spiral galaxy J2345-0449 (with AGN jets) is also located (Bagchi et al. 2014; Nesvadba et al. 2021). NGC 1961 and NGC 6753 are located at the lower end of star forming galaxies’ main sequence.

UGC 12591 is one of the rare, most peculiar galaxies in the Universe having very high rotational velocities at around 500 km s^{-1} (Giovanelli et al. 1986), almost twice of the rotational velocity of the Milky Way and one of the fastest measured till date. UGC 12591 is isolated and the nearest satellite galaxy to it is 1.09 Mpc away. Reda et al. (2004) discuss possible scenarios of formation of the early-type isolated galaxies like early epoch collapse, merging event, accretion etc. The dust lanes of UGC 12591 indicates a past merging or accretion event.

Any merging event has drastic effect on the shape and size of the parent galaxy as well as its star formation. In most cases the star formation is triggered due to collision (Sanders et al. 1988) and takes place in the nuclear region of $10^2 - 10^3 \text{ pc}$ of the galaxy. If there is no hot halo then the galaxy becomes bulge dominated after merger. Otherwise, hot halo helps in inflow of the cold gas which again helps in the regrowth of the disk by increasing SFR as shown by Kannan et al. (2015). In contrast to that Moster et al. (2011) did a study on the star forming efficiency during mergers and find that the presence of a hot halo reduces the efficiency of star formation as compared to absence of a hot halo during the merging event. Dai et al. (2012) using XMM-newton detected a hot gaseous halo in UGC 12591. So, it can be said that there was a time when the galaxy might have gone through higher star formation rate. But from SED fitting it is inferred that the total mass of the young stars is negligibly small. That indicates the recent SFR ($t_{\text{age}} < 10^8 \text{ years}$) is extremely low and the object most probably has crossed an era of violent quenching

of its star formation. How this remarkable quenching of star formation could have happened early in its evolutionary history and why star formation did not resume at later stages are still open issues which needs more detailed study. Nevertheless, We discuss some possibilities;

The reason for the low star formation rate in early-type galaxies like UGC 12591 could also be related to AGN activity of central black hole (further discussed below), or related to the structural properties. Martig et al. (2013) finds that early-type galaxies form stars 2-5 times less efficiently than the spirals due to the reason that gas discs of early-types are more stable against star formation because of which they do not create high density clumps capable of star formation. Morganti et al. (2005) show that radio-loud phase of AGN activity can hamper the star formation by heating up the interstellar gas making it metal rich. Dekel & Burkert (2014) describes two mechanisms for the suppression of star formation in massive galaxies; internal quenching by a compact bulge, specifically at high red shifts, and quenching due to hot halos at low red-shift.

3.5 Central black hole mass and AGN feedback

Here we investigate the possible quenching of star formation due to growth of a supermassive black hole. The mass and accretion state of this black hole are key factors which decide its radiative or kinetic influence on the surrounding medium. We estimated the nuclear black hole mass from the tight $M_{\text{bh}} - \sigma_c$ relation for a sample of E, S0 and

S types of galaxies as given in Gültekin et al. (2009), following the equation,

$$\log\left(\frac{M_{\text{bh}}}{M_{\odot}}\right) = \alpha + \beta \log\left(\frac{\sigma_c}{200 \text{ km s}^{-1}}\right) \quad (4)$$

This relation is calibrated using dynamically detected central black hole masses and has an intrinsic rms scatter of $\epsilon = 0.44 \pm 0.06$. Here $\alpha = 8.12 \pm 0.08$ and $\beta = 4.24 \pm 0.41$ and σ_c is the central velocity dispersion, taken as $288.0 \pm 23.9 \text{ km s}^{-1}$ from HyperLEDA (Makarov et al. 2014)². The black hole mass is obtained as $M_{\text{bh}} = 6.18 \times 10^8 M_{\odot}$ within the range of $3.18 \times 10^8 M_{\odot}$ to $1.25 \times 10^9 M_{\odot}$. UGC 12591 being a highly bulge dominated galaxy, the $M_{\text{bh}} - \sigma$ relation should give a good estimate of the black hole mass (Kormendy & Ho 2013).

Sahu et al. (2019) analysed a sample of 84 early-type galaxies with directly measured SMBH masses and show how black hole mass is tightly scaled to spheroidal as well as total stellar masses. For UGC 12591 if we use $M_{\text{bh}} = 6.18 \times 10^8 M_{\odot}$ then we obtain its spheroid/bulge stellar mass $M_{\star, \text{sph}} = 4.4 \times 10^{10} M_{\odot}$ and total galaxy stellar mass $M_{\star, \text{gal}} = 1.1 \times 10^{11} M_{\odot}$ (Sahu et al. (2019, Eq. 12,14)). This estimate of $M_{\star, \text{gal}}$ brackets the stellar mass calculated from SED fitting in the range $9.5 \times 10^{10} - 1.6 \times 10^{11} M_{\odot}$ and $M_{\star, \text{sph}}$ mass is close to our estimate of V band bulge mass (Table 4, 5 and Table 6). This shows that UGC 12591 hosts a massive black hole of $\approx 1.4\%$ of bulge mass while $\approx 28 - 46\%$ of the total stellar mass resides in the bulge itself, consistent with the highly bulge dominated nature of UGC 12591.

The above black hole mass M_{bh} is in the range of super massive black holes, reasonable enough for a massive bulged galaxy like UGC 12591. The origin and growth of a black hole within a galaxy this massive remains an unsolved problem (Kormendy & Ho 2013). Even though the sphere of influence of a black hole is small when compared to the size of a galaxy, a SMBH can effectively regulate the star formation within the galaxy. It has been found that more massive is the bulge more massive is the black hole and the host galaxy will be more redder in colour. In addition, the black hole may have a powerful effect on the evolution of a galaxy, although there is no good observational corroboration of the fact. However, recently Martín-Navarro et al. (2018) from a study on a group of 74 massive galaxies obtained a striking correlation between the black hole mass and star formation rate of the galaxy. The galaxies with over massive black holes have SFR which is quenched much earlier than the SFR of the galaxies with under massive black holes. At the same time, the galaxies with over massive black holes had more star formation going on at a faster rate in the past than the other category of galaxies. They conclude that the higher baryon cooling efficiency at high redshift would play a major role in growth of supermassive black holes, feeding the primordial seeds of the black holes with gas and forming more stars, in agreement with quasar observations at higher redshifts. The stellar mass formed at $z \approx 5$ in over-massive black-hole galaxies is about 30% more than those in under-massive black-hole galaxies.

Finding clues from its present properties, we propose that progenitor of UGC 12591 may have gone through an intense starburst phase in the past. The subsequent suppression of the star formation in the galaxy was possibly mediated by the intense AGN activity of the growing SMBH. From SED fitting we found that this SMBH at the present moment is quiescent, i.e. neither we see large ($> 1 \text{ kpc}$) radio jets nor is the black hole contributing significantly to the mid-

IR flux, ruling out the presence of strong radiative feedback from a bright AGN. This, and absence of large radio jets implies possible feedback of this AGN is via small-scale jets ($< 1 \text{ kpc}$) or uncollimated winds/outflows powered by low Eddington rate, hot accretion flow on the SMBH (Yuan & Narayan 2014).

However, there is a strong possibility that $\gtrsim 10^9$ yrs back (maximum lifetime of quasars/radio galaxies) this galaxy had passed through a phase in which the accretion rate of matter around the black hole was high, resulting in far stronger AGN activity giving rise to energetic outflows (in quasar mode) or powerful relativistic jets (in radio mode) which made the environment of the galaxy hostile of forming new stars. Numerical simulation results of black hole growth via mergers in early Universe match this scenario (Di Matteo et al. 2005). Recent CO observations of a massive, Mpc-jet launching spiral J2345-0449 showing strong SFR quenching (Nesvadba et al. 2021) and state-of-the-art relativistic hydrodynamic simulations of jets propagating in a dense ISM (Mukherjee et al. 2016; Mandal et al. 2021) provide good support for this scenario, while future radio and X-ray telescopes have great potential of revolutionizing this field (Nyland et al. 2018).

Other than AGN activity there are other methods discussed in literature by which the star formation can be quenched. Khoperskov et al. (2018) finds that the presence of a stellar bar can effectively reduce the star formation by a factor of 10 in less than 1 Gyr time. Martig et al. (2009) suggest ‘morphological quenching’, where in early-type galaxies the quenching of star formation can result from growth of a stellar spheroid/bulge by mergers. During the transition of stellar disk to spheroidal shape, strong shear boosted by the steep gravitational potential gradients of their bulges may lower SFR in such galaxies.

3.6 Baryon census in relation to the galaxy halo mass and SFR

3.6.1 The Baryonic Tully-Fisher relation

The Baryonic Tully-Fisher relation (BTFR; McGaugh et al. (2000); McGaugh (2005)) is a remarkably tight power-law correlation connecting the baryonic mass and the circular rotational velocity (halo mass) of spiral galaxies which is measured to follow a single power-law over a very wide range in galaxy mass, e.g. (Bell & de Jong 2001; Lelli et al. 2016b; Verheijen 2001; Papastergis et al. 2016; Geha et al. 2006; Ponomareva et al. 2021). Currently, the origin of BTFR is not fully understood, but it holds the key to understanding galaxies as physical objects, their dark-matter, baryon and stellar content, and most importantly, how they formed.

The BTFR can be expressed in the following way,

$$M_{\text{bar}} = \gamma v_{\text{rot}}^{\beta} \quad (5)$$

Where, M_{bar} is the total baryonic mass of the galaxy, which includes the mass of the stars, M_{\star} and mass of the gases, M_{gas} (molecular, atomic and ionized). Here γ is the normalising parameter and β is the slope in the linearised equation using logarithmic scale.

SED fitting for UGC 12591 has yielded the stellar mass, $M_{\star} = 1.6 \times 10^{11} M_{\odot}$ and the gas mass $M_{\text{gas}} = 7.0 \times 10^{10} M_{\odot}$ (Table 4). Now in order to also include the atomic HI gas mass of the galaxy, the following equation has been used,

$$M_{\text{HI}} = 2.356 \times 10^5 \times D_L^2 \times (1+z)^{-2} \times \int F dv \quad (6)$$

Here, M_{HI} is the HI mass in M_{\odot} , D_L is the luminosity distance

² <http://leda.univ-lyon1.fr/>

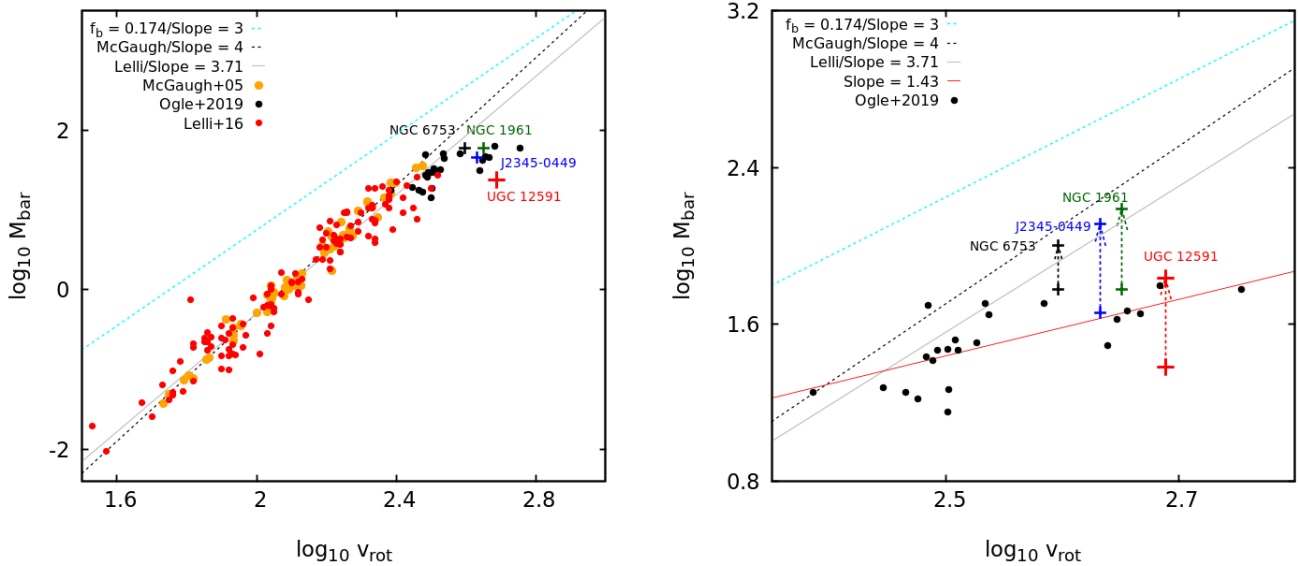


Figure 7. In these plots the baryonic mass and the rotational velocity of UGC 12591 is compared to some other galaxies. Left: A baryonic Tully-Fisher (BTF) relation is shown, where M_{bar} is the baryonic mass in units of $10^{10}M_{\odot}$ and v_{rot} is the maximum (flat) rotational velocity in km s^{-1} . Galaxy data from [McGaugh \(2005\)](#) and [Lelli et al. \(2016a\)](#) are plotted with the linear fit in lower rotation velocity/mass regime $\approx v_{\text{rot}} \lesssim 300 \text{ km s}^{-1}$ deriving similar slopes of 4.00 and 3.71 respectively (dashed and solid lines). The data for highly rotating, massive super-spirals from [Ogle et al. \(2019b\)](#) have also been plotted (black points), where most of the galaxies have rotational velocities $> 300 \text{ km s}^{-1}$. The rotational velocity of UGC 12591 is taken as 488.4 km s^{-1} from Hyperleda ([Makarov et al. 2014](#)). We find that the tight, linear BTF relation starts to turn over (flatten) for galaxies with highest v_{rot} , implying a significant baryonic shortfall in massive halos, which is also mentioned in [Dai et al. \(2012\)](#), [Ogle et al. \(2019b\)](#) and [Courtois et al. \(2015\)](#). In these plots the radio-loud (hosting Mpc scale radio jets) spiral galaxy J2345-0448 is a rare exception where significant mass of the cosmic baryons are found (see Fig. 8) in an luminous, extended hot X-ray halo ([Bagchi et al. 2014](#); [Mirakhor et al. 2021](#); [Walker et al. 2015](#)). Right: Here we fit the super-spiral sample from [Ogle et al. \(2019b\)](#) along with UGC 12591 and other massive spiral galaxies J2345-0449, NGC 1961 ([Anderson et al. 2016](#)) and NGC 6753 ([Bogdán et al. 2013](#)) to find out how much their BTFR slope is differing from that in the linear regime of lower mass galaxies in left figure. The slope is 1.43 ± 0.31 , which is much flatter compared to $\sim 3.7 - 4$. For the four most massive galaxies mentioned, the upper data points are total baryonic mass, including the hot gas component and the lower points represent the ‘condensed’ baryonic mass, excluding the hot gas budget. The baryonic masses of hot gas components are estimated within the virial radius of the galaxies from published X-ray observations. It can be seen that after inclusion of hot X-ray halo baryons in J2345-0449, NGC 1961 and NGC 6753, they all fall exactly on the BTF relation of slope $\sim 3.7 - 4$. On the contrary, UGC 12591 still falls much below of that line even after including the hot halo gas mass extrapolated upto its virial radius. In both the plots we have shown the $M_{\text{bar}} \propto v_{\text{rot}}^3$ power law (the light-blue dotted line) for cosmic baryon fraction $f_b = 0.174$ following [McGaugh \(2012\)](#); [Lelli et al. \(2016b\)](#).

in Mpc and $\int F dv$ is the integrated HI line flux in the unit of Jy km s^{-1} . Using $\int F dv = 2.45 \text{ Jy km s}^{-1}$ and D_L as 97.5 Mpc, the total HI gas mass (M_{HI}) is estimated at $5.2(\pm 1.6) \times 10^9 M_{\odot}$. The uncertainty in HI mass is obtained by the method suggested by ([Doyle & Drinkwater 2006](#)). Adding contribution of Helium and metals into account, we consider $M_{\text{He}} + M_{\text{HI}} = 1.33 \times M_{\text{HI}}$, yielding $M_{\text{He}} + M_{\text{HI}} = 6.92(\pm 2.1) \times 10^9 M_{\odot}$. The HI mass is high but in the region of most massive galaxies, with $M_{\text{HI}}/M_{\star} \sim 0.04$ and beyond the break at $M_{\star} \sim 10^9 M_{\odot}$ on the $M_{\text{HI}} - M_{\star}$ plane ([Maddox et al. 2015](#)).

Summing up all this baryonic census with the X-ray halo hot gas mass $M_{\text{gas,hot}}$ of $4.5 \times 10^{11} M_{\odot}$, taken as upper limit within 500 kpc from the centre of the galaxy from [Dai et al. \(2012\)](#), the total baryonic mass of the galaxy becomes $6.87 \times 10^{11} M_{\odot}$. In Fig. 7, we have plotted both the total baryonic mass with hot gas contribution and without hot gas on the BTFR along with different samples of galaxies mentioned in figure caption. Two best fitting lines of the form $M_{\text{bar}} \propto v_{\text{rot}}^{\beta}$ are also shown as determined by ([McGaugh 2005](#)) ($\beta = 4.0$) and ([Lelli et al. 2016a](#)) ($\beta = 3.71$). We further discuss the implications of BTFR below.

3.6.2 Where are most of the baryons in super massive ($> L_{\star}$) galaxies?

Generally the baryons census around massive $> L_{\star}$ local galaxies reveal much less observable baryons than that is expected from Big Bang nucleosynthesis and Cosmic Microwave Background constraints (see [Tumlinson et al. \(2017\)](#) for a review). Previous studies have shown (albeit for a handful of galaxies so far) that only a small fraction ($\sim 10 - 30\%$) of these ‘missing baryons’ are located in the warm-hot ($\sim 10^6 \text{ K}$) circum-galactic corona around the massive galaxies, possibly extending upto the virial radius of their dark matter halos ([Dai et al. 2012](#); [Mirakhor et al. 2021](#); [Walker et al. 2015](#); [Anderson & Bregman 2011](#); [Anderson et al. 2016](#); [Bregman et al. 2018](#); [Bogdán et al. 2013](#)). UGC 12591 is an excellent target to probe the ‘missing baryon’ problem because it is unusually massive and situated in a low density environment which causes lower interaction with the intra-cluster medium and other galaxies.

The position of most massive spiral galaxies on the Baryonic Tully-Fisher relation should provide some fundamental insights into the missing baryon problem and galaxy formation. The remarkably tight baryonic Tully-Fisher relation ([Lelli et al. 2016b](#)) shown in Fig. 7 of slope $3.7 - 4.0$ connecting M_{bar} , the total baryonic mass of the galaxies and the halo mass, represented by v_{rot} the maximum

rotational velocity, implies that on an average a nearly constant fraction (~ 0.4) of all baryons expected in a halo are “condensed” onto the disc of rotationally supported galaxies (Zaritsky et al. 2014). The dashed blue line shows the Λ CDM prediction assuming that galaxies contain all available cosmological baryons. A constant slope ($\beta \sim 4$) and remarkable tightness of BTFR suggest a self-similar scaling mechanism for rotating discs operating across a wide range of halo masses. However, it has been suspected (Dai et al. 2012; Ogle et al. 2019b; Courtois et al. 2015) that for highest mass $L > L_\star$ galaxies ($M_\star \gtrsim 10^{11} M_\odot$) the linear BTF relation starts to turn over/flatten at highest v_{rot} , implying a significant baryonic shortfall of massive galactic discs. This part of the BTFR has remained the least studied so far. We reexamine and confirm this trend as shown in Fig. 7 by including UGC 12591 and some of the most massive disc galaxies known in the literature. For these galaxies the derived BTFR slope is 1.43 ± 0.31 , which is much flatter compared to $\sim 3.7 - 4$, for lower mass halos.

Furthermore, We find that when the expected baryonic mass from a linear fitted BTFR of slope ~ 4 is assumed to be present in UGC 12591, and assume $M_{200} = 1.9 \times 10^{13} M_\odot$ (Dai et al. 2012), we can restore the galaxy’s baryonic mass fraction up to $f_b = 0.147$, near to the cosmological closure value 0.17. In that case about four times more baryonic mass possibly resides in an extended galactic halo than what has been observed so far in all wavelengths, including the X-ray halo (Fig. 7 right panel). Thus, to account for these so called ‘missing baryons’ we have to admit that there is a baryon shortfall of $\sim 75\%$ in this galaxy. We show in Fig. 7 that a similar baryon shortfall with respect to the linear BTFR is also indicated for NGC 1961, NGC 6753, J2345-0449 and for several other highly rotating, massive super-spirals taken from Ogle et al. (2019b). We show that after inclusion of hot X-ray halo baryons observed in J2345-0449, NGC 1961 and NGC 6753, they all fall exactly on the BTF relation of slope $\sim 3.7 - 4$. On the contrary, UGC 12591 still falls much below of that line even after including the hot halo gas mass extrapolated upto its virial radius. Many phenomenon can drive the baryon loss of galaxies such as supernova blowout, AGN feedback via a quasar mode wind or a via powerful radio jets, as reviewed in Tumlinson et al. (2017).

Now, why the most massive galaxies may deviate from the tight, linear fitting BTFR law? One interesting possibility why the linear BTFR breaks/flattens for most massive halos is because a comparatively lesser fraction of halo baryons in these galaxies are able to condense into discs and form new stars or form massive neutral hydrogen discs, as we find in this work and further discussed below (Section 3.6.4). This could indicate a deviation or perturbation in the self-similar scaling relation due to non-gravitational processes such as AGN feedback, supernova blowout, bulge formation or a longer radiative cooling time of baryons in CGM. Interestingly, Sabater et al. (2019) showed that the central SMBH in most massive galaxies ($M_\star > 10^{11} M_\odot$) are always switched on at various levels of AGN activity in radio wavelengths, in line with models in which these AGN are essential for maintaining the quenched state of galaxies at the centres of hot gas haloes. It remains to be seen if this departure from linear BTFR is a generic feature for most massive galaxies, using more data on these rare giants. This is a powerful clue, as the exact physical process inhibiting star formation in massive rotating discs is still unclear and this signal presents an outstanding challenge for future investigations.

The rotation curve for UGC 12591 is constrained to be flat only within about 40 kpc from the nucleus (Giovannelli et al. 1986). Rotation curves are the major tools for determining the mass distribution in spiral galaxies, e.g. (Sofue & Rubin 2001). If a flat rotation

curve and Kepler’s law is assumed to hold true upto 80 kpc from the centre (the maximum extent of soft X-ray halo), then one can obtain an interior gravitational mass $M_{g,\text{tot}} = 4.44 \times 10^{12} M_\odot$, i.e. $M_{\text{xray-halo}} \sim 0.1 M_{g,\text{tot}}$ within 80 kpc. Accounting for the baryonic mass of the hot X-ray halo $M_{\text{gas,hot}}$ of $4.5 \times 10^{11} M_\odot$ and the total baryonic mass in disc found from our SED-fitting, one can estimate the baryonic fraction to be $f_b = 0.155$ which is close to the cosmological mean value of 0.174 (Spergel et al. 2007). Thus, within the X-ray halo radius, the baryon fraction is near closure and significant fraction of these baryons reside in a hot gaseous phase, rather forming stars.

One should treat this result with caution as the HI rotation curve of UGC 12591 has not been measured upto 80 Kpc from the center and we have no information about the distribution of dark matter mass $M_{g,\text{tot}}$. Future spatially resolved, deep 21cm radio observations may measure the rotation curve more accurately, probing the gravitational potential, as well as it may reveal the anomalous HI gas structures (rings, outflows, warps) with high angular resolution at the outskirts of this galaxy.

What is the total mass budget within R_{200} ? From a tight correlation between black hole mass and the total gravitational mass found by (Bandara et al. 2009) the gravitational mass within virial radius ($R_{200} \approx 550$ kpc) M_{200} can be calculated from the following,

$$\log M_{\text{bh}} = (8.18 \pm 0.11) + (1.55 \pm 0.31)[-13 + \log(M_{200}/M_\odot)] \quad (7)$$

To use this correlation we need the central black hole mass. Now, using the M_{bh} obtained from the $M - \sigma$ relation and its scatter, we obtain the total halo mass $M_{200} = 2.47 \times 10^{13} M_\odot$, within the range of $1.6 \times 10^{13} M_\odot$ to $3.9 \times 10^{13} M_\odot$. This mass is close to the value calculated by Dai et al. (2012) of $M_{200,\text{xray}} = 1.9 \times 10^{13} M_\odot$ from the X-ray halo data assuming hydro-static equilibrium condition. If one uses this value of M_{200} and use observed M_{bar} , then the estimate of mass fraction in baryons is only ~ 0.03 out to R_{200} , as against the cosmological value ~ 0.17 , which is extremely puzzling. The baryon mass budget reads; total baryon mass $4.2 \times 10^{12} M_\odot$, observed baryon mass $6.87 \times 10^{11} M_\odot$, and yet-to-be observed baryon mass $3.51 \times 10^{12} M_\odot$. This $\sim 80\%$ ‘missing baryon’ mass (or possibly the missing light) discrepancy creates a tension with the standard models of galaxy formation (White & Rees 1978; White & Frenk 1991; Fukugita & Peebles 2006; Sommer-Larsen 2006) which demand a hot X-ray corona containing a large fraction (at least 50%) of cosmic baryons, thus bringing us face-to-face to the most important question: where do most of the undetected cosmic baryons in UGC 12591 reside and in what form?

There are several possibilities; (a) The hot corona of UGC 12591 is not in hydrostatic equilibrium, giving an erroneous estimate of M_{200} . This can not be ruled out as yet and it would mean that the halo gas is dynamically unstable, either expanding outwards or collapsing inwards. However, If the X-ray halo gas is in virial equilibrium, it will attain the virial temperature of (T_{vir}), corresponding to the depth of gravitational potential well and exhibit Keplerian rotational (virial) velocity v_{rot} :

$$T_{\text{vir}}(\text{eV}) = 34.47 \times (v_{\text{rot}}/100 \text{ km s}^{-1})^2 \quad (8)$$

For $v_{\text{rot}} = 400 - 500 \text{ km s}^{-1}$ (halo mass $\sim 10^{13} M_\odot$) we find $T_{\text{vir}} = 0.5 - 0.8 \text{ keV}$, quite close to the measured X-ray value $T_{\text{xray}} \approx 0.64 \pm 0.03 \text{ keV}$ (Dai et al. 2012). If not a coincidence, the X-ray halo gas is in virial equilibrium of a massive dark matter halo of total mass $\text{few} \times 10^{13} M_\odot$ as suggested by Dai et al. (2012). This in turn implies the halo gas is possibly shock heated after being accreted

from the cosmic-web rather than recycled from the disc. The thermal and metal line cooling time of the quasi-hydrostatic X-ray halo gas is large, in the range 2.8 – 6.3 Gyr for material within the cooling radius, and has the effective cooling rate of $0.15 - 0.21 M_{\odot} \text{ year}^{-1}$ (Fukugita & Peebles 2006; Dai et al. 2012; Kelly et al. 2021). The average estimated cooling time is much larger than the free-fall time, and therefore, it would require more than a Hubble time to build the entire stellar mass of galaxy by condensation of cooling gas from halo, thus disfavoring such a possibility.

(b) a large deposit of cosmic baryons is yet to be found within R_{200} and possibly beyond. What is the state (density, temperature and metal content) of these baryons? The X-ray corona of all the over massive spirals detected so far show a trend of declining temperature profile, and beyond virial radius most likely their gas temperature would be below $< 10^6$ K where EUV and FUV wavelengths provide the best diagnostics. These baryons may exist in a cold and low density phase which makes it very difficult to observe them with current X-ray telescopes, hence these are prime targets for future highly promising exploratory missions (Simionescu et al. 2021; Bregman et al. 2018; Nicastro et al. 2021).

Another possibility (c) is that actual M_{200} is far smaller than above, as we require only $\approx 4 \times 10^{12} M_{\odot}$ to resolve the tension with cosmological baryon fraction. If true this would imply that possibly all the baryons are present within ~ 100 kpc; $\sim 4.5 \times 10^{11} M_{\odot}$ ($\sim 66\%$) in the X-ray halo and $\sim 2.4 \times 10^{11} M_{\odot}$ ($\sim 34\%$) in stars and ISM, and the rest is dark matter of mass $\sim 3.3 \times 10^{12} M_{\odot}$. In that case the rotation curve may show a steep decline in the halo region if measurable so far out. Since there are no robust observational estimates of M_{200} as yet, one can not rule out this possibility. However in the widely accepted standard cosmological paradigm we expect the most massive galaxies to form in most massive halos dominated by dark matter and a massive dark matter halo has a strong dynamical and stabilizing influence on the disc. We again emphasize that the total halo mass of UGC 12591 is the crucial parameter that is not well constrained, since it also depends on extrapolation of the observed rotation curve or X-ray gas profile to R_{200} .

3.6.3 Baryons in UGC 12591 and Super-Spirals

Super spirals are an interesting newly discovered galaxy population which are extremely massive, fast rotating HI-rich disc galaxies with significantly high star forming rates (Ogle et al. 2019b). In terms of rotation velocity a few of them approach or even exceed the v_{rot} for UGC 12591. In Fig. 6 and Fig. 7 we have included the super spiral sample of Ogle et al. (2019b). We find that compared to the super-spirals which all lie close to the main sequence of star formation, UGC 12591 has a strikingly low star formation rate. Ogle et al. (2019b) note that super-spirals show a break in the BTFR at mass limit of $> \log(M_{\star}/M_{\odot}) \sim 11.5$ (see Fig. 7). UGC 12591 confirms to the same trend with its $\log(M_{\star}/M_{\odot}) \sim 11.2$ and it falls in the region of highest mass super spirals, well beyond the break in the linear BTFR, which is quite evident from the figure. This indicates that the present SFR of a galaxy does not have a major effect on its position on the baryonic Tully-Fisher plane but it is the total baryon mass which is most important.

As discussed in § 3.4 that in the past UGC 12591 may have had a starburst phase which has been quenched exponentially over time. The main reason for a galaxy to stop forming stars is the unavailability of the necessary light elements like hydrogen and helium in its cloud. So, the small star formation rate indicates the presence of more abundance of metallic elements in its gaseous clouds which could have been thus enriched due to past supernova explosions in the disc

which in turn may have blown out baryons in the halo of the galaxy. In future a sensitive spectroscopic measurement of metal abundance of the baryons in the circum galactic halos will be necessary to test this model (see Simionescu et al. (2021); Nicastro et al. (2021) and a review by Tumlinson et al. (2017)).

3.6.4 Condensed Baryon Fraction and Baryons to Stars Conversion Efficiency

For reasons still unclear, massive local galaxies like UGC 12591 have low specific star formation rate compared to other less massive spirals (see Wechsler & Tinker (2018) for a review). However, interestingly, Posti et al. (2019) in a study of nearby star-forming galaxies with M_{\star} ranging from $10^7 - 10^{11} M_{\odot}$ found that some massive spirals with $M_{\star} \gtrsim 10^{11} M_{\odot}$ have turned most of the baryons in their halos into stars, without being subjected much to the quenching processes and there are hardly any missing baryons in them (see also Zhang et al. (2021)).

The star formation efficiency of a galaxy, f_{\star} , can be expressed by,

$$f_{\star} = \frac{M_{\star}}{M_{\text{halo}}} \frac{\Omega_{\text{m}}}{\Omega_{\text{b}}} \quad (9)$$

For UGC 12591 If we take halo mass $M_{\text{halo}} = M_{200}$ as calculated in § 3.6.1 and stellar mass $M_{\star} = 1.6 \times 10^{11} M_{\odot}$ we get $f_{\star} \sim 0.04$ in the range 0.02-0.06, for universal cosmic baryon fraction $\frac{\Omega_{\text{b}}}{\Omega_{\text{m}}} = 0.174$. This shows that in spite of a very large halo mass it is able to convert only a small fraction (2–6%) of halo baryons to stars. On the contrary, the sample of most massive spirals with $M_{\star} = 1 - 3 \times 10^{11} M_{\odot}$ of Posti et al. (2019) yields $f_{\star} \approx 0.3 - 1$ which shows their high efficiency of star formation and their stellar baryon fraction is approaching the cosmological baryon fraction. Although a very interesting result, it is still too early to tell if these unusual spirals of Posti et al. (2019) have experienced the same evolutionary and SFH as the majority of normal spirals.

UGC 12591 appears to be very different because of its very low f_{\star} and possibly most of the cosmic baryons may reside in the dark matter halo, unable to turn into stars. Now if we insert total baryonic mass (§ 3.6.1) instead of stellar mass in Eq. 9 assuming all the baryons could have been converted to stars, we find $f_{\star} \sim 0.16$, again highlighting the stark star formation deficiency of this galaxy. Li et al. (2018) estimate the baryon budget of the hot circum galactic medium of six local isolated massive spiral galaxies, including UGC 12591, finding that a significant amount of the ‘missing baryons’ are possibly stored beyond the virial radius of their dark matter halos and not condensing into stars. Although such large repository of baryons beyond the virial radius is not yet found in any galaxy, if true, this may explain the insufficiency of the hot baryons inside virial radius to account for the expected cosmic baryons. These baryons may enable galaxies to continue forming stars steadily for long periods of time and account for missing baryons in galaxies in the local universe, but for most massive galaxies like UGC 12591 we find just the opposite. This finding is broadly consistent with the constraints from abundance matching techniques to determine the typical galaxy stellar mass at a given halo mass. The simulations show that peak efficiency of f_{\star} is always fairly quite low, at $z = 0$ reaching a peak of about 20 – 30% for typical L_{\star} galaxies with halo mass $M_{200} \sim 10^{12} M_{\odot}$. Beyond the peak f_{\star} declines rapidly to $f_{\star} \sim 2 - 5\%$ at $M_{200} \sim 10^{13} M_{\odot}$ (Behroozi et al. 2010, 2019; Moster et al. 2013). It is believed that AGN feedback is one of the main ingredients needed to bring this decline in SFR, e.g. (Di Matteo et al. 2005; Beckmann et al. 2017).

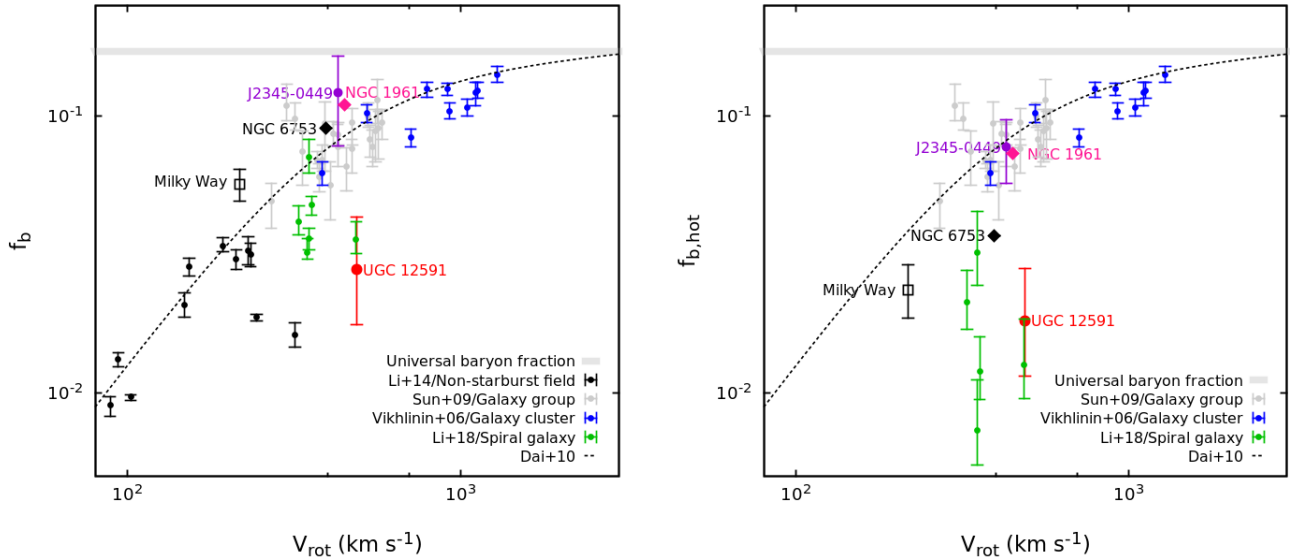


Figure 8. The baryon fractions of galaxies, groups and clusters with different rotational velocities have been shown along with UGC 12591. The left plot shows fraction of all baryons f_b and the right plot shows the baryon fraction only in hot halo phase $f_{b,\text{hot}}$ relative to the cosmic baryon fraction (horizontal grey zone $0.167 - 0.174$; [Spergel et al. \(2007\)](#); [Komatsu et al. \(2009\)](#)). The data points consist of non-starburst field spirals ([Li et al. 2014](#)), spirals from [Li et al. \(2018\)](#), galaxy groups of [Sun et al. \(2009\)](#), galaxy clusters ([Vikhlinin et al. 2006](#)) and the Milky way ([Miller & Bregman 2015](#)) with their uncertainties. The dotted line represents the power law model between f_b and v_{rot} presented by [Dai et al. \(2010\)](#). For comparison another extremely massive and fast rotating spiral galaxy J2345-0449 has been shown on these graphs ([Bagchi et al. 2014](#); [Mirakhor et al. 2021](#); [Walker et al. 2015](#)) that is seen to lie on the edge of the cosmic baryon fraction. Massive spirals like NGC 1961 ([Anderson et al. 2016](#)) and NGC 6753 ([Bogdán et al. 2013](#)) can also be seen to be in the nearby region of cosmic baryon fraction. In contrast UGC 12591 falls far below the universal baryon fraction line, as it has baryon fraction out to R_{200} of only ≈ 0.028 within the range of $0.018 - 0.043$, showing a baryon deficiency of $\sim 80\%$, signaling a large tension with cosmological predictions.

To probe further the tension of baryon budget of UGC 12591 and standard cosmology we may compare it with the baryon fraction of massive halos, including galaxy groups and clusters. In left panel Fig. 8 we plot the fraction of all baryons, f_b (in stars + ISM + hot halo gas), and the right panel shows the baryon fraction only in hot halo phase, $f_{b,\text{hot}}$, relative to the cosmic baryon fraction (the horizontal grey zone). Here the rotation velocity v_{rot} is used as proxy for the total mass of the halo. Now we see that the progressive increase of f_b at higher v_{rot} , which approaches the cosmic value for cluster mass halos, indicating that most massive halos are nearly at closure for baryonic matter, compared to average galaxies such as the Milky Way and even the most massive galaxies. In baryon budget the stellar mass component begins to dominate for galaxy mass halos while group and clusters are largely dominated by hot gas phase. In spite its large halo mass we find a striking lack of baryon fraction in UGC 12591, even after including those contained in its X-ray halo (Fig. 8 right plot). The hot baryon fraction $f_{b,\text{hot}}$ still remains significantly lower than inferred from X-ray observations of galaxy groups with similar v_{rot} .

On the contrary, the extremely massive, rapidly rotating, relativistic-jet-launching spiral galaxy J2345-0449 ([Bagchi et al. 2014](#); [Nesvadba et al. 2021](#)) is an interesting and rare exception, which has the baryon mass fraction within the virial radius (~ 450 kpc) of $f_b = 0.121 \pm 0.043$ ([Mirakhor et al. 2021](#); [Walker et al. 2015](#)), similar to the universal baryon fraction of group mass halos and has similar hot gas fraction (Fig. 8 right plot). NGC 1961 and NGC 6753 are also close to it in terms of their baryonic budget. Although the halo mass of UGC 12591 is close to that of NGC 1961, NGC 6753 and J2345-0449, in terms of baryon content in hot halo, it falls short of these other three remarkable galaxies.

Next we compare the 0.5-2 keV band X-ray luminosity (L_x) of all known massive spiral galaxies with detected soft X-ray halos. We find that at $L_x = 4.0 \pm 0.5 \times 10^{41}$ erg s $^{-1}$ the luminosity of J2345-0449 is highest ([Mirakhor et al. 2021](#)), about 10 times that of UGC 12591 ([Dai et al. 2012](#)), NGC 6753 ([Bregman et al. 2018](#); [Bogdán et al. 2013](#)) and significantly higher than that of NGC 1961 ([Anderson et al. 2016](#)). The metal abundance of UGC 12591 halo is low at $\sim 0.1Z_{\odot}$, similar to those found for J2345-0449, NGC 1961 and NGC 6753. This metallicity is consistent with baryon deficit, low metallicity coronal gas around massive galaxies shown in EAGLE hydro simulations ([Kelly et al. 2021](#); [Schaye et al. 2015](#)). Although the halo mass of UGC 12591, NGC 1961, NGC 6753 and J2345-0449 are similar, the higher X-ray luminosity and the larger extent of J2345-0449 corona (about 160 kpc, or 35 per cent of r_{200}) is still intriguing. We point out that J2345-0449 is the only one of those four galaxies which hosts large scale radio jets. Therefore, possibly it is a consequence of powerful Mpc scale radio jets and past supernovae activity in this galaxy, heating ([Nesvadba et al. 2021](#)) and expelling the inner baryons upto a larger radius and preventing gas cooling in the halo, although more observational proof is needed to demonstrate this scenario robustly.

4 SUMMARY

In this paper we analyse the structure of an extremely fast rotating and massive, early-type or hybrid (S0/a) galaxy UGC 12591 by fitting PSF convolved 2D surface brightness models to HST/WFC3 images in the three bands of F160W (H), F814W (I) and F606W (V). In all of three bands a two component fit, viz Sersic and exponential-disk, yields

satisfactory results but adding one more component of PSF function optimizes the model further and improves the residuals. UGC 12591 is found to be a bulge dominated galaxy with Sersic index n ranging from 2.32–3.68, effective bulge radius r_e in $7.35''$ – $12.32''$ (3.3–5.6 kpc) and the disk scale length r_s in $41.56''$ – $58.43''$ (18.8–26.4 kpc) in V, I and H bands, respectively.

We have calibrated the spectral energy distribution of the galaxy using two powerful softwares, namely CIGALE and MAGPHYS. SED fitting by CIGALE gives total stellar mass of $1.6 \times 10^{11} M_\odot$ with the ratio of old to young stellar mass as high as 1.6×10^5 . The instantaneous star formation rate of $0.11 M_\odot \text{yr}^{-1}$ and specific star formation rate, $6.6 \times 10^{-13} \text{yr}^{-1}$ indicates extreme quenching and near absence of recent star forming activity in the galaxy. We discussed where it stands compared to other massive galaxies in the same mass range and the possible effect of structural bulge and AGN activity in the past in lowering the star formation. The SED fitting values of CIGALE are well consistent with the results of MAGPHYS where we got stellar mass of $9.5 \times 10^{10} M_\odot$, SFR $0.28 M_\odot \text{yr}^{-1}$ and sSFR $3 \times 10^{-12} \text{yr}^{-1}$.

UGC 12591 possesses both an extended ellipsoidal stellar bulge, and a giant equatorial disc of gas and dust. The fraction of total infrared dust luminosity contributed by the ISM dust is as high as 90%, with total dust luminosity $L_{\text{dust}} = (0.5 - 3.5) \times 10^{10} L_\odot$, dominated by cold dust at equilibrium temperature $T_C \approx 15\text{K}$. The total dust mass in ISM is estimated at $4.10 \times 10^8 M_\odot$, much higher than normal spiral galaxies.

Virial mass within R_{200} is calculated as $2.47 \times 10^{13} M_\odot$ which is close to previous gravitational mass calculated from X-ray observations, assuming a hydrostatic equilibrium state for the hot X-ray corona. Having included the XMM-Newton detected X-ray halo mass in the baryonic budget, and accounting for all ISM and stellar baryons from SED fitting, we find total baryonic mass of $6.87 \times 10^{11} M_\odot$ for UGC 12591. This corresponds to total baryon fraction ~ 0.03 , far less than cosmological baryonic closure value, and amounting to a baryon deficiency of $\sim 80\%$ within the virial radius. However, within 80 kpc (the X-ray halo radius) the baryon fraction is ~ 0.16 , taking total gravitational mass as $4.4 \times 10^{12} M_\odot$. This value is near the cosmological baryon fraction which is ~ 0.17 . This implies that only a small fraction of these cosmic baryons reside in a galaxy scale halo and about five times more baryonic mass possibly resides in the extended circum galactic halo and filaments than what has been observed so far in all wavelengths.

On the Baryonic Tully Fisher relation plot we show UGC 12591 falls far below the well established linear relation of slope ~ 4 . All other known fast rotating and massive spirals like J2345-0449, NGC 1961, NGC 6753 and other super massive spirals also follow the same trend. After inclusion of hot X-ray halo baryons detected in J2345-0449, NGC 1961 and NGC 6753, they all fall exactly on the classic BTF relation of slope $\sim 3.7 - 4$. On the contrary, UGC 12591 still falls much below of that line even after including the hot halo gas mass extrapolated upto its virial radius. This could indicate a deviation or breakdown in the self-similar scaling relation governing BTFR due to some non-gravitational processes such as AGN feedback, supernova blowout, bulge formation or a longer radiative cooling time of baryons in CGM, due to some heating process.

UGC 12591 is found host to a super massive black hole of mass $6.18 \times 10^8 M_\odot$ which at the present moment is quiescent, i.e., neither we see large scale ($> 1\text{kpc}$) radio jets nor is the black hole contributing significantly to the mid-IR SED, ruling out the presence of strong radiative feedback from a bright AGN. A compact central radio source having 1.4 GHz luminosity of $L_{1.4} = 3.01 \pm 0.92 \times 10^{32} \text{W}$ is found which can possibly be attributed to radio emission of an

AGN. Possible role of intense AGN activity and energetic feedback of this black hole in the past, in quenching the star formation activity is discussed.

In this paper we showed that a super massive and highly star formation quenched, fast rotating spiral galaxy like UGC 12591 is extremely unusual. Indeed, UGC 12591 is one of the rare, most massive such galaxies known in the local universe. Because it is not obvious how this galaxy acquired such a range of extraordinary properties, it poses many challenges to theoretical models. Further investigations via multi-wavelength observations of it hold the key for understanding the coevolution of black holes and massive disk galaxies, the strong quenching of star formation, the complex interplay of dark-matter and baryonic physics taking place in massive halos, and the role played by AGN feedback and bulge formation in its evolution, which will help in explaining the unique characteristics displayed by this galaxy.

ACKNOWLEDGEMENTS

SR gratefully acknowledges the support from IUCAA under the student visiting program and funding by Indian Space Research Organisation (ISRO) under 'AstroSat Data Utilization' project. JB acknowledges the support from Department of Physics and Electronics, CHRIST (Deemed to be University), Bangalore. SD acknowledges the support from Department of Science and Technology (DST), New Delhi under the INSPIRE faculty Scheme (sanctioned No: DST/INSPIRE/04/2015/000108). MBP gratefully acknowledges the support from following funding schemes: The Science and Engineering Research Board (SERB), New Delhi under the SERB "SERB Research Scientists Scheme" Scheme and Indian Space Research Organisation (ISRO) under 'AstroSat Data Utilization' project. MBP, JJ and BKG acknowledge the support from IUCAA Associateship program. This research has made use of the data from *HST* Archive. Part of the reported results is based on observations made with the NASA/ESA Hubble Space Telescope, obtained from the Data Archive at the Space Telescope Science Institute, which is operated by the Association of Universities for Research in Astronomy, Inc., under NASA contract NAS 5-26555. This research has made use of NASA's Astrophysics Data System, and of the NASA/IPAC Extragalactic Database (NED) which is operated by the Jet Propulsion Laboratory, California Institute of Technology, under contract with the National Aeronautics and Space Administration. We have used images and results from SDSS and funding for SDSS has been provided by the Alfred P. Sloan Foundation, the participating institutions, the National Science Foundation, and the U.S. Department of Energy's Office of Science. This research has made use of the NASA/IPAC Extragalactic Database (NED) which is operated by the Jet Propulsion Laboratory, California Institute of Technology, under contract with the NASA. Facilities: HST (ACS), SDSS.

DATA AVAILABILITY

The data used in this paper are publicly available at <https://hla.stsci.edu>. The retrieved data used in the analysis are tabulated in Table. 1 and Table. 2. The code used in reducing the HST observations is publicly available at <https://users.obs.carnegiescience.edu/peng/work/galfit/galfit.html>, <http://www.iap.fr/magphys/>, and <https://cigale.lam.fr>.

REFERENCES

- Anderson M. E., Bregman J. N., 2011, *ApJ*, **737**, 22
- Anderson M. E., Churazov E., Bregman J. N., 2016, *MNRAS*, **455**, 227
- Bagchi J., et al., 2014, *ApJ*, **788**, 174
- Bandara K., Crampton D., Simard L., 2009, *ApJ*, **704**, 1135
- Beckmann R. S., et al., 2017, *MNRAS*, **472**, 949
- Behroozi P. S., Conroy C., Wechsler R. H., 2010, *ApJ*, **717**, 379
- Behroozi P., Wechsler R. H., Hearin A. P., Conroy C., 2019, *MNRAS*, **488**, 3143
- Bell E. F., de Jong R. S., 2001, *ApJ*, **550**, 212
- Bendo G. J., et al., 2015, *MNRAS*, **448**, 135
- Bertin E., Arnouts S., 1996, *A&AS*, **117**, 393
- Bogdán Á., et al., 2013, *ApJ*, **772**, 97
- Boquien M., Burgarella D., Roehly Y., Buat V., Ciesla L., Corre D., Inoue A. K., Salas H., 2019, *A&A*, **622**, A103
- Bregman J. N., Anderson M. E., Miller M. J., Hodges-Kluck E., Dai X., Li J.-T., Li Y., Qu Z., 2018, *ApJ*, **862**, 3
- Bruzual G., Charlot S., 2003, *MNRAS*, **344**, 1000
- Burgarella D., Buat V., Iglesias-Páramo J., 2005, *MNRAS*, **360**, 1413
- Condon J. J., Cotton W. D., Greisen E. W., Yin Q. F., Perley R. A., Taylor G. B., Broderick J. J., 1998, *AJ*, **115**, 1693
- Condon J. J., Cotton W. D., Broderick J. J., 2002, *AJ*, **124**, 675
- Courtois H. M., Zaritsky D., Sorce J. G., Pomarède D., 2015, *MNRAS*, **448**, 1767
- Dai X., Bregman J. N., Kochanek C. S., Rasia E., 2010, *ApJ*, **719**, 119
- Dai X., Anderson M. E., Bregman J. N., Miller J. M., 2012, *ApJ*, **755**, 107
- Dale D. A., Helou G., Magdis G. E., Armus L., Díaz-Santos T., Shi Y., 2014, *ApJ*, **784**, 83
- Dekel A., Burkert A., 2014, *MNRAS*, **438**, 1870
- Di Matteo T., Springel V., Hernquist L., 2005, *Nature*, **433**, 604
- Doyle M. T., Drinkwater M. J., 2006, *MNRAS*, **372**, 977
- Elbaz D., et al., 2007, *A&A*, **468**, 33
- Fabian A. C., 2012, *ARA&A*, **50**, 455
- Federrath C., Klessen R. S., 2012, *ApJ*, **761**, 156
- Fisher D. B., Drory N., 2008, *AJ*, **136**, 773
- Fukugita M., Peebles P. J. E., 2006, *ApJ*, **639**, 590
- Gebhardt K., et al., 2000, *ApJ*, **539**, L13
- Geha M., Blanton M. R., Masjedi M., West A. A., 2006, *ApJ*, **653**, 240
- Giovanelli R., Haynes M. P., Rubin V. C., Ford W. K. J., 1986, *ApJ*, **301**, L7
- Gültekin K., et al., 2009, *ApJ*, **698**, 198
- Häring N., Rix H.-W., 2004, *ApJ*, **604**, L89
- Hoopes C. G., et al., 2007, *ApJS*, **173**, 441
- Inoue A. K., 2011, *MNRAS*, **415**, 2920
- Kalinova V., Colombo D., Sánchez S. F., Kodaira K., García-Benito R., González Delgado R., Rosolowsky E., Lacerda E. A. D., 2021, *A&A*, **648**, A64
- Kannan R., Macciò A. V., Fontanot F., Moster B. P., Karman W., Somerville R. S., 2015, *MNRAS*, **452**, 4347
- Kelly A. J., Jenkins A., Frenk C. S., 2021, *MNRAS*, **502**, 2934
- Kennicutt Robert C. J., 1998, *ApJ*, **498**, 541
- Khoperskov S., Haywood M., Di Matteo P., Lehnert M. D., Combes F., 2018, *A&A*, **609**, A60
- Komatsu E., et al., 2009, *ApJS*, **180**, 330
- Kormendy J., Ho L. C., 2013, *ARA&A*, **51**, 511
- Lanz L., Ogle P. M., Alatalo K., Appleton P. N., 2016, *ApJ*, **826**, 29
- Lelli F., McGaugh S. S., Schombert J. M., 2016a, *AJ*, **152**, 157
- Lelli F., McGaugh S. S., Schombert J. M., 2016b, *ApJ*, **816**, L14
- Li J.-T., Crain R. A., Wang Q. D., 2014, *MNRAS*, **440**, 859
- Li J.-T., Bregman J. N., Wang Q. D., Crain R. A., Anderson M. E., Zhang S., 2017, *ApJS*, **233**, 20
- Li J.-T., Bregman J. N., Wang Q. D., Crain R. A., Anderson M. E., 2018, *ApJ*, **855**, L24
- Lynden-Bell D., 1969, *Nature*, **223**, 690
- MacArthur L. A., Courteau S., Holtzman J. A., 2003, *ApJ*, **582**, 689
- Madau P., Dickinson M., 2014, *ARA&A*, **52**, 415
- Maddox N., Hess K. M., Obreschkow D., Jarvis M. J., Blyth S. L., 2015, *MNRAS*, **447**, 1610
- Magorrian J., et al., 1998, *AJ*, **115**, 2285
- Makarov D., Prugniel P., Terekhova N., Courtois H., Vauglin I., 2014, *A&A*, **570**, A13
- Mandal A., Mukherjee D., Federrath C., Nesvadba N. P. H., Bicknell G. V., Wagner A. Y., Meenakshi M., 2021, *MNRAS*, **508**, 4738
- Marconi A., Hunt L. K., 2003, *ApJ*, **589**, L21
- Martig M., Bournaud F., Teyssier R., Dekel A., 2009, *ApJ*, **707**, 250
- Martig M., et al., 2013, *MNRAS*, **432**, 1914
- Martín-Navarro I., Brodie J. P., Romanowsky A. J., Ruiz-Lara T., van de Ven G., 2018, *Nature*, **553**, 307
- McGaugh S. S., 2005, *ApJ*, **632**, 859
- McGaugh S. S., 2012, *The Astronomical Journal*, **143**, 40
- McGaugh S. S., Schombert J. M., Bothun G. D., de Blok W. J. G., 2000, *ApJ*, **533**, L99
- Meiksin A., 2006, *MNRAS*, **365**, 807
- Miller M. J., Bregman J. N., 2015, *ApJ*, **800**, 14
- Mirakhor M. S., et al., 2021, *MNRAS*, **500**, 2503
- Möllenhoff C., 2004, *A&A*, **415**, 63
- Morganti R., Tadhunter C. N., Oosterloo T. A., 2005, *A&A*, **444**, L9
- Moster B. P., Macciò A. V., Somerville R. S., Naab T., Cox T. J., 2011, *MNRAS*, **415**, 3750
- Moster B. P., Naab T., White S. D. M., 2013, *MNRAS*, **428**, 3121
- Mukherjee D., Bicknell G. V., Sutherland R., Wagner A., 2016, *MNRAS*, **461**, 967
- Nesvadba N. P. H., et al., 2010, *A&A*, **521**, A65
- Nesvadba N. P. H., et al., 2021, *A&A*, **654**, A8
- Nicastro F., et al., 2021, *Experimental Astronomy*, **51**, 1013
- Noll S., Burgarella D., Giovannoli E., Buat V., Marcillac D., Muñoz-Mateos J. C., 2009, *A&A*, **507**, 1793
- Nyland K., et al., 2018, *ApJ*, **859**, 23
- Ogle P. M., Lanz L., Appleton P. N., Helou G., Mazzarella J., 2019a, *The Astrophysical Journal Supplement Series*, **243**, 14
- Ogle P. M., Jarrett T., Lanz L., Cluver M., Alatalo K., Appleton P. N., Mazzarella J. M., 2019b, *ApJ*, **884**, L11
- Orellana G., et al., 2017, *A&A*, **602**, A68
- Papastergis E., Adams E. A. K., van der Hulst J. M., 2016, *A&A*, **593**, A39
- Peng C. Y., Ho L. C., Impey C. D., Rix H.-W., 2002, *AJ*, **124**, 266
- Ponomareva A. A., et al., 2021, *MNRAS*, **508**, 1195
- Posti L., Fraternali F., Marasco A., 2019, *A&A*, **626**, A56
- Reda F. M., Forbes D. A., Beasley M. A., O’Sullivan E. J., Goudfrooij P., 2004, *MNRAS*, **354**, 851
- Roberts M. S., 1978, *AJ*, **83**, 1026
- Rowlands K., et al., 2012, *MNRAS*, **419**, 2545
- Sabater J., et al., 2019, *A&A*, **622**, A17
- Sahu N., Graham A. W., Davis B. L., 2019, *ApJ*, **876**, 155
- Salim S., et al., 2016, *ApJS*, **227**, 2
- Sanders D. B., Soifer B. T., Elias J. H., Madore B. F., Matthews K., Neugebauer G., Scoville N. Z., 1988, *ApJ*, **325**, 74
- Schaye J., et al., 2015, *MNRAS*, **446**, 521
- Simionescu A., et al., 2021, *Experimental Astronomy*, **51**, 1043
- Sofue Y., Rubin V., 2001, *ARA&A*, **39**, 137
- Somerville R. S., Davé R., 2015, *ARA&A*, **53**, 51
- Somerville R. S., Hopkins P. F., Cox T. J., Robertson B. E., Hernquist L., 2008, *MNRAS*, **391**, 481
- Sommer-Larsen J., 2006, *ApJ*, **644**, L1
- Spergel D. N., et al., 2007, *ApJS*, **170**, 377
- Sun M., Voit G. M., Donahue M., Jones C., Forman W., Vikhlinin A., 2009, *ApJ*, **693**, 1142
- Tody D., 1986, in Crawford D. L., ed., *Society of Photo-Optical Instrumentation Engineers (SPIE) Conference Series Vol. 627, Instrumentation in astronomy VI*. p. 733. doi:10.1117/12.968154
- Tody D., 1993, in Hanisch R. J., Brissenden R. J. V., Barnes J., eds, *Astronomical Society of the Pacific Conference Series Vol. 52, Astronomical Data Analysis Software and Systems II*. p. 173
- Tumlinson J., Peebles M. S., Werk J. K., 2017, *ARA&A*, **55**, 389
- Verheijen M. A. W., 2001, *ApJ*, **563**, 694
- Vikhlinin A., Kravtsov A., Forman W., Jones C., Markevitch M., Murray S. S., Van Speybroeck L., 2006, *ApJ*, **640**, 691

- Vogelsberger M., Marinacci F., Torrey P., Puchwein E., 2020, [Nature Reviews Physics](#), **2**, 42
- Walker S. A., Bagchi J., Fabian A. C., 2015, [MNRAS](#), **449**, 3527
- Wall R. E., Kilic M., Bergeron P., Rolland B., Genest-Beaulieu C., Gianninas A., 2019, [MNRAS](#), **489**, 5046
- Wechsler R. H., Tinker J. L., 2018, [ARA&A](#), **56**, 435
- White S. D. M., Frenk C. S., 1991, [ApJ](#), **379**, 52
- White S. D. M., Rees M. J., 1978, [MNRAS](#), **183**, 341
- Yuan F., Narayan R., 2014, [ARA&A](#), **52**, 529
- Zaritsky D., et al., 2014, [AJ](#), **147**, 134
- Zhang Z., Wang H., Luo W., Zhang J., Mo H. J., Jing Y., Yang X., Li H., 2021, arXiv e-prints, p. [arXiv:2112.04777](#)
- da Cunha E., Charlot S., Elbaz D., 2008, [MNRAS](#), **388**, 1595
- da Cunha E., Eminian C., Charlot S., Blaizot J., 2010, [MNRAS](#), **403**, 1894

This paper has been typeset from a $\text{\TeX}/\text{\LaTeX}$ file prepared by the author.